Simulations of complex crack paths using a robust and cost-efficient continuous–discontinuous approach

Amar El Ouazani Tuhami, Sylvia Feld-Payet, Stéphane Quilici, Nikolay Osipov, Jacques Besson

Simulations of complex crack paths using a robust and cost-efficient continuous-discontinuous approach

A. El Ouazani Tuhami[a,c], S. Feld-Payet[b,*], S. Quilici[c], N. Osipov[c], J. Besson[a]

[a] *Mines Paris, PSL University, Centre for material sciences (MAT), UMR7633 CNRS, 91003 Evry, France*
[b] *DMAS, ONERA, Université Paris Saclay, F-92322 Châtillon — France*
[c] *Transvalor, S.A. 950 Avenue Roumanille — CS 40237 Biot — 06904 Sophia Antipolis Cedex, France*

Abstract

Prediction of complex crack propagation is necessary to guarantee performance in service of critical parts of transport vehicles despite the presence of a crack. In cases where linear fracture mechanics assumptions are not valid, e.g. for ductile rupture, this prediction may require continuous-discontinuous strategies to insert a strong discontinuity (*i.e.* a crack) into a continuous model based on a scalar variable related to material degradation. These strategies still face difficult challenges regarding robustness and cost-efficiency, in particular for 3D problems. To overcome these challenges, it is useful to consider the different ingredients that constitute a continuous-discontinuous strategy and try to optimize each of them. With this perspective, this work addresses the simulation of crack initiation and propagation in ductile metals and proposes new contributions to some rarely addressed points: (i) a simple geometrical approach to initiate realistic crack

*Corresponding author
URL: sylvia.feld-payet@onera.fr (S. Feld-Payet)

FEM: Finite Element Method; GTN: Gurson-Tvergaard-Needleman; XFEM: eXtended Finite Element Method; APZ: Active Process Zone(s); SPR: Super–convergent Patch Recovery.

shapes in 3D meshes, (ii) a new 3D insertion criterion to minimize the number of transfer operations, (iii) a pragmatic remeshing procedure to refine only Active Process Zones, and (iv) an equilibrium recovery method meant to improve the convergence rate after the insertion of a discontinuity.
The effectiveness of these new ingredients is demonstrated in 2D axisymmetric, 2D plane strain, and 3D cases in the case of test specimens used to characterize ductile failure in metals. This includes axisymmetric specimens exhibiting cup-cone fracture, plane strain specimens with slant fracture, and pre-cracked CT-like specimens with crack blunting and large crack propagation.
Keywords: Mesh adaption; Crack path tracking; Ductile failure; Cup-cone failure; Slant crack path.

---

1. Introduction

When designing critical parts of transport vehicles, it is necessary to guarantee performance in service despite the presence of a crack. To do so, it is important to properly predict crack propagation, which can result in non-trivial crack paths (*i.e.* with deflection, branching, ...). When complex crack propagation cannot be predicted by linear fracture mechanics, it can be interesting to use continuum damage mechanics models describing local material degradation phenomena. These continuous models are all the more appealing that they have the advantage of enabling to predict crack initiation. However, continuum damage mechanics models also have their limits. On the one hand, they cannot provide an accurate estimation of the opening and growth kinetics of the crack [1]. On the other hand, the propagation length may be limited by the computational size of the continuous model if it requires a fine discretization [2]. This may be particularly

problematic when using regularized methods [3–7] to simulate the ductile rupture of large industrial structures. Indeed, these regularization methods are required to avoid pathological mesh dependency [8–10], but they necessitate a refinement of the mesh inside localization bands. To overcome these problems related to the accurate description of cracks and the need for fine meshes, several strategies consisting in inserting a strong discontinuity in the finite element model, based on the material degradation field, have been proposed in the literature for ductile failure.

In [11], the authors combined a continuous damage model regularized with an implicit gradient formulation with an anisotropic mesh adaption strategy to describe ductile failure up to crack initiation. The remeshing procedure was driven by an error estimator based on damage and damage rate. Then, a simple element erosion technique was used to represent the crack path, while avoiding stretched elements near the crack tip. The proposed strategy was applied to simulate the cup-cone fracture of a pre-notched specimen under tensile loading with a 3D mesh. However, the considered mesh was refined over the whole crack path, which brings the issue of large computational size. In addition, the crack path resulting from a simple element erosion was indented, without any guarantee of continuity, and the bandwidth of the removed element was not controlled.

In [12], a similar strategy was proposed but applied with a local continuous damage model with parameters identified for a given minimum mesh size. A 3D bi-section local h—adaptive remeshing procedure was combined with a hybrid FEM-Diffuse field transfer technique with improved point selection in order to optimize remeshing computational cost. Although no regularization technique

has been used, the remeshing procedure is not efficient for industrial simulations either due to the refinement of the mesh along the entire crack path: this leads to an increase of the computational size of the problem with the crack length. Besides, since the erosion technique was also used for crack representation, the crack path was also indented.

In [13], a continuous damage model regularized with an implicit gradient method was used in combination with a remeshing procedure to not only avoid element distortion occurring at high strains, but also to represent the discrete crack. The direction of crack propagation was defined thanks to an extension to 3D simulations of the crack path tracking algorithm introduced in [14]. Besides, a method capable of initiating 3D cracks in the volume or near the body surface was developed. Simulations in 3D displaying simple crack paths were presented. However, the proposed method using the smoothed local maximum search over different radii to track crack paths is not capable of detecting crack branching.

In [15], the authors considered a multi-surface continuous model with internal necking and damage mechanisms under shear solicitations. An implicit gradient method was applied to regularize the problem. For damage to crack transition, cohesive bands were inserted between the element interfaces using the discontinuous Galerkin framework. The position and insertion time of the cohesive band was determined using bifurcation analysis. This strategy was applied to simulate cup-cone and slant fracture on 2D meshes. However, as the cohesive elements were introduced at the elements' interfaces, the resulting crack path was mesh-dependent. Moreover, a fine mesh was once again used along the entire crack path, which results in a high computational cost.

In [16], the authors used a local continuous GTN model to describe material

degradation in the elements up to the point of localization. This point was either defined by the occurrence of plastic instability indicated by a bifurcation type analysis, or by having reached a critical porosity value associated with void coalescence. Then, depending of the case, the orientation of the crack in each selected element was determined either directly by the bifurcation criterion or by an additional criterion combining the directions of localization for mode I and mode II driven coalescence. In the end, the selected direction for a given element might also depend on the directions found for the neighbouring elements and on the crack intersections with adjacent elements to ensure a continuous crack propagation. The authors then used a coupling of the eXtended Finite Element Method (known as XFEM [17]) and Cohesive Zone Method for crack representation. A simulation of 3D cup–cone crack path was showcased using a coarse mesh. Although the use of a coarse mesh was interesting to reduce the computational cost, its association with the choice to entirely cut an hexahedral element into two parts, or to not cut it at all, limits the accuracy of the crack front. Finally, as noted by the authors, it would be necessary to extend this methodology to the finite strain framework since ductile failure involves important geometrical changes.

In a more recent work [18, 19], the authors proposed a phase-field approach coupled with remeshing and discrete crack insertion by adaptive remeshing. The main contribution of this work was the development of a crack path tracking algorithm and crack insertion method based on remeshing adapted for parallel computations. The capacities of the developed algorithm (also known as CIPFAR: Crack Insertion and Propagation using the Phase Field and Adaptive Remeshing) were illustrated for 3D meshes of 3 flat specimens with and without notches. It

is important to note that the proposed methodology to identify the crack surface intersection locations relies on the evolution of the damage gradient along any sufficiently damaged edges. This local search does not guarantee the continuity of the crack surface nor a smooth front. Besides, in this evolution, the contribution of the damage gradient along the crack propagation direction is also taken into account: this restricts the application of this method in areas where damage is sufficiently high to make this contribution negligible.

In order to compare different continuous-discontinuous strategies and be able to take advantage of the interesting parts in the different propositions to reach a specific goal, it is useful to distinguish the elementary components of these rather complex strategies. That is why the first section of this paper aims at exposing the different ingredients that make up a continuous-discontinuous strategy. This facilitates the choice of the best option for each ingredient, with regard to the desired objective. In this paper, the authors' objective is to be able to perform efficient simulations of complex 3D crack path advance over long distances with an accurate description of the crack at a reasonable cost. To do so, new contributions on rarely addressed points are proposed, viz.: (i) a simple geometrical approach to initiate realistic crack shapes in 3D meshes, (ii) a new 3D insertion criterion to minimize the number of transfer operations, (iii) a pragmatic remeshing procedure to refine only Active Process Zones (APZ), and (iv) an equilibrium recovery method meant to improve the convergence rate after the insertion of a discontinuity. The complete strategy is described in section 3, with more details on the new contributions. Although this paper proposes generic numerical contributions for the continuous–discontinuous

transition, it is necessary, in order to illustrate the principles and evaluate the robustness of the proposed numerical tools, to consider real application cases. As this work addresses failure of ductile media, the implicit gradient Gurson-Tvergaard-Needleman (GTN) model with two characteristic lengths proposed by the authors in [10] is used within a finite strain framework. This model is able to describe all three stages of ductile failure within a finite strain framework and is especially suited to model complex crack paths such as the one associated with cup cone failure. However, the proposed contributions could be used, with slight adjustments, in combination with different constitutive models. That is why the considered constitutive equations are only briefly recalled in Appendix A. The gain in robustness and cost efficiency offered by the proposed contributions is evaluated in section 4. Finally, the ability of the proposed strategy to capture complex crack paths, such as cup-cone and slant failure, or deal with challenging simulations, is illustrated in section 5 on several 2D and 3D cases.

The implementation of the proposed algorithms and the simulations were performed with the Z-set software [20, 21]. A fully implicit resolution scheme is used.

2. Preliminary considerations and literature overview

In this section, the elementary components of a continuous-discontinuous strategy to simulate ductile crack propagation are presented. The choices made for the present strategy are specified. The new contributions are situated with respect to the existing propositions in the literature.

2.1. Building a continuous-discontinuous strategy

A continuous-discontinuous strategy can be defined by four features:

— a discontinuity representation method;

— a methodology to define where to insert a crack increment;

— a criterion to determine when to insert a crack increment;

— a procedure to retrieve equilibrium after the model has been changed due to the insertion of a crack increment.

For each item, different options are available in the literature, that can be combined depending on the user's needs and requirements (a review of the options can be found in [22]). In particular, the authors' aim is to be able to model complex 3D crack propagation in ductile media while providing an accurate description of the crack. This objective already motivated the propositions of Feld-Payet *et al.* [23, 24], which serve as a basis for this work. However, in this paper, the authors aim to go further by tackling long crack propagation within a large strain framework, with a particular emphasis on keeping the computational costs reasonable. These new constraints call for new solutions, described in the following.

2.2. Representation of the discontinuity

The choice of the discontinuity representation is the same as in [23, 24], *i.e.* mesh adaption, for three main reasons.

The first one is that mesh adaption enables to describe accurately the crack geometry thanks to a discrete representation. In the present case, the crack geometry is first defined independently of the structure's mesh. Then the crack mesh is inserted in the computational mesh using a robust cutting algorithm [25] followed by additional refinement operations to improve element quality. Let

us note that XFEM would also provide an accurate discrete representation. In this last case, an implicit representation of the crack surface is often considered thanks to level set functions as introduced by Stolarska *et al.* [26]. As the crack advances, these level set functions would then need to be updated through various techniques, notably described in [27]. Both representation choices, *i.e.* mesh adaption and XFEM, would lead to a more accurate and realistic representation than the element erosion technique.

The second reason is that, contrary to XFEM, mesh adaption also avoids element distortion due to large deformations (especially right ahead of the crack front), which is common in ductile media.

The third reason is that mesh adaption ensures a reasonable quality/cost ratio by enabling both to refine the elements in the damage process zone before crack insertion (to properly capture the nonlocal damage evolution) and then to increase the element size after crack opening. This coarsening of the mesh in the damage process zone after the passage of the crack constitutes, with the fact that mesh adaption is performed here on the current configuration, two original elements compared to the previous work [23, 24]. In the end, only a small zone of the computational mesh contains fine elements thanks to the proposed procedure described in section 3.4.2 to track the Active Process Zone.

2.3. Strategy to define where to insert a crack

The second element of a continuous-discontinuous strategy regards the means to determine where a crack should be inserted. If the choice of crack representation requires knowing the position of a continuous hypersurface, then it is necessary to define a criterion to specify the crack increment orientation. This criterion can either rely on a vector field (*e.g.*, obtained from stability and

bifurcation analyses [15], or from an eigenvalue decomposition of stress or strain tensors [28, 29]) or on a scalar field presenting a ridge on the crack location. In both cases, a difficult point is that this orientation criterion considers discrete data often available at the integration points. In order to build a crack path from these data that is not only continuous but also sufficiently regular, efficient crack path tracking algorithms are required.

Among the most effective methods to impose more regularity, very few enable to capture simultaneously two crack branches without *a priori* knowing the number of branches: the Crack Path Field of Oliver *et al.* [30] as used by Lloberas-Valls *et al.* [31], the Marching Ridges proposed by Feld-Payet *et al.*[23, 24] and the simplified Medial Axis Method of Tamayo-Mas *et al.* [32, 33]. This characteristic is essential when simulating cup cone failure [34] since two competing branches appear after the initial crack growth stage at high stress triaxiality. The Marching Ridges algorithm is used in this paper since, contrary to the Crack Path Field, there is no choice to be made for the projection vector and contrary to the simplified Medial Axis Method, it does not require that the crack should start at a boundary or that the damage distribution should be symmetric with respect to the crack surface. Besides, the Marching Ridges algorithm only considers an underlying spatial scalar field representing material degradation. As it use only local information near the crack front, the associated computational cost is negligible compared to the FEM computation. This low computational cost is essential for a procedure like the one proposed as it is called after each converged load increment.

In the end, the Marching Ridges algorithm provides, for each point discretizing the current crack front, a vector that is tangent to the crack

propagation direction. For three-dimensional problems, this piece of information is exploited to build a three-dimensional crack representation adapted to the chosen method to represent the discontinuity. For an explicit representation, *i.e.* a mesh of the crack surface, this can be simply done by paving each crack increment with triangular elements between the points that discretize the current front and the ends of the tangent vectors. However, this piece of information could also be exploited to build an implicit representation as well.

Whatever the crack representation choice, one of the most challenging situations to model is crack initiation completely inside the volume (*i.e.* away from any boundary) in three dimensions. This issue is hardly treated in the literature, so there are only a few references on the subject to the authors' knowledge. The first difficulty is determining the position of a point of the first crack increment. To do so, Feld-Payet *et al.* [23, 24] and Javani *et al.* [13] have proposed to use a weighted average of the points where critical damage has been exceeded. Then, Javani *et al.* [13] considered the longest vector connecting the barycenter to the farthest point in the cloud of selected points. From here, a second vector was needed to define a crack initiation surface: this vector could be either the longest projected vector in the normal plane from all the considered points or the closest node on the surface. Mirroring these two vectors finally led to the diagonals of a rectangular first crack increment. Feld-Payet *et al.* [24] have also proposed to build a rectangular first increment by using, this time, the Marching Ridges algorithm in three given orthogonal planes, corresponding to the global frame and considering two intersections. In order to reduce the computational cost induced by three different analyses with the Marching Ridges algorithm and to provide a more robust crack position by taking into account more points than for

both previously mentioned options, the authors here propose, for this very little discussed subject, a new solution presented in section 3.2.1.

2.4. Criterion to define when to insert a crack

Once the direction of the crack increment is determined, it is necessary to choose a criterion to determine whether this increment should be inserted. The choice of this criterion strongly depends on the constitutive equations. In this work, a regularized GTN model able to represent cup–cone failure proposed in [10] is used. Since this is a coupled damage model (*i.e.* degradation impacts the material response) and since the authors use mesh adaption techniques to insert a crack directly (*i.e.* without inserting a cohesive zone to describe final failure), a crack increment should be only inserted when the degradation variable is locally sufficiently important so that the material has almost lost its load carrying capacity. Insertion of a cohesive zone would enable to insert a crack increment before complete failure to concentrate final degradation on a surface. However, this would require the definition of a softening function. This is more usual for discontinuity insertion in an undamaged medium in quasi-brittle 2D-like problems [35, 36], but more challenging for damaged materials, especially if an equivalence of dissipation with a continuous damage model is expected for mixed-mode failure within a 3D framework [37].

However, a more or less extended area can have reached this critical degradation state. Therefore, the next question is to determine the size of the crack increment to be inserted, which is linked to the insertion frequency. On the one hand, regularly inserting small crack increments should allow being sufficiently representative of the crack advance at a high cost. On the other hand, inserting larger increments at a lower frequency should reduce the computational cost at

the risk of being unable to retrieve equilibrium after remeshing. A compromise between these two approaches must be found. To the authors' knowledge, this question is rarely tackled in the literature, especially for the three-dimensional case. The choice of Feld-Payet *et al.* [23, 24] was to impose a unique user-defined crack length and to only allow crack insertion when the degradation state would enable the insertion of all the crack increments along the front. This assumption is unsuitable for non-straight crack fronts. Consequently, another option suitable for more general cases is proposed in section 3.3.3.

2.5. Procedure to retrieve equilibrium after insertion

After the insertion of the discontinuity, the model has been locally changed in particular in the case of a discrete crack representation. This means that, whether one uses XFEM or mesh adaption, transfer operations are required before resuming computation. These operations necessarily introduce some errors since no transfer operator can guarantee to respect at the same time the kinematical relations, the equilibrium equations and the boundary conditions (while minimizing diffusion of course). The transfer operations can lead to difficulties to retrieve equilibrium. It is then necessary to, at least, enable time step division as Boroomand et Zienkiewicz [38] and Feld-Payet et al. [23, 24], which results in an increasing number of increments and thus larger computational costs. A few propositions exist in the literature to help retrieve equilibrium:

— Transfer of only a few selected variables and use of local relations to compute the rest, as proposed by Camacho et Ortiz [39], Mediavilla [40] or Broumand *et al.* [41];

— Introduction of an elastic step with the boundary conditions of the current

increment, as proposed by Mediavilla in [40];

— Introduction of a relaxation step with vanishing boundary conditions, as proposed by Broumand *et al.* [41], Javanmardi and Maheri [42] or Seabra *et al.* [43].

In section 3.6, the authors propose a new contribution which is inspired by Mediavilla's proposition to use the current boundary conditions, but involves using the complete constitutive behavior to also adjust plasticity and damage.

2.6. Prerequisites on the continuous model

The starting point of any continuous-discontinuous strategy is a continuous model describing material degradation. The only requirements for the model, given the previously mentioned choices, are:

— There should be a continuous scalar field (*e.g.* f, $D, \dots$) representing material degradation (since the Marching Ridges algorithm is considered);

— It is possible to estimate a critical value (*e.g.* f_{crit}, $D_{\text{crit}}, \dots$) of the considered variable corresponding to complete material degradation (in other words, a material point reaching this critical value can be considered as *broken*);

— Material degradation is more or less localized in a band of width l_b;

— The problem should be regularized (since mesh adaption is performed).

For the considered nonlocal GTN model, the best scalar field candidate is the total porosity f_t. Theoretically, the porosity at failure should be equal to $f_R = 1/q_1$ where q_1 is a parameter used to tune the void growth kinetics. In practice, to

facilitate convergence, material degradation is assumed complete for a critical value f_{crit} very close to f_R: $f_{\text{crit}} = \eta/q_1$ with $0.95 \leq \eta \leq 1$ (in this range, the choice of η has little influence on the overall behavior but convergence is easier when $\eta \neq 1$). In the present case, the coefficient η is set to 0.95 and thus one has $f_R = 0.63$, according to the chosen material parameters reported in table A.2.

3. Continuous–discontinuous damage transition strategy

3.1. Summary of the strategy

The chosen continuous–discontinuous damage transition strategy can be summarized by the following choices:

— Representation of the crack as a strong discontinuity in the mesh using mesh adaption. Mesh adaption is also used to produce optimal meshing: (i) before crack initiation, the map size of the mesh is set by the user and actualized after a chosen time increment $\Delta t_{\text{remeshing}}$ to prevent element distortion, (ii) after crack initiation, an automatic mesh refinement of the Active Process Zone is carried out, which guarantees mesh coarsening in already cracked zones;

— Strategy to define where to insert a crack increment: two cases need to be considered: (i) crack initiation for which a new strategy for 3D cases is proposed, (ii) crack propagation where the Marching Ridges algorithm is used.

— Criterion to determine when to insert a crack increment: a new criterion based on the crack increment surface is proposed;

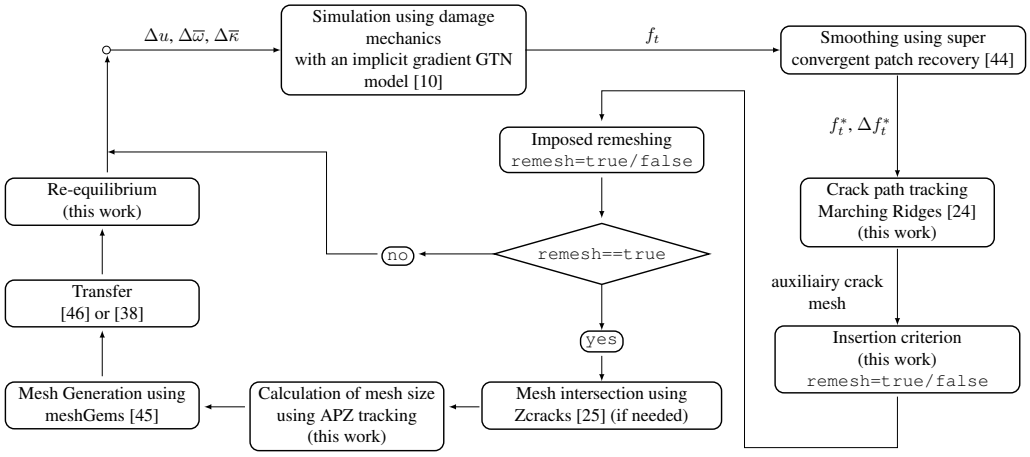

Figure 1: Flowchart describing the proposed continuous—discontinuous approach with the different involved components and their inputs/outputs.

— Procedure to retrieve equilibrium after the model has been changed due to the insertion of crack increments: transfer with finite element interpolation for nodal data, and nearest integration point association for integration points data and a new re-equilibrium procedure consisting in relaxation steps using the material behavior for a few increments as opposed to an elastic step re-equilibrium technique where only the elastic behavior is considered.

Each component of the proposed procedure is detailed in the following. The sequence of the corresponding operations is represented in figure 1.

3.2. Where to insert a crack increment?

To define the location of a continuous and sufficiently regular crack surface, the Marching Ridges Algorithm introduced in [23, 24] is chosen in this work for the crack propagation phase and for crack initiation in 2D. However, although this algorithm provides a unified way to deal with crack propagation and crack

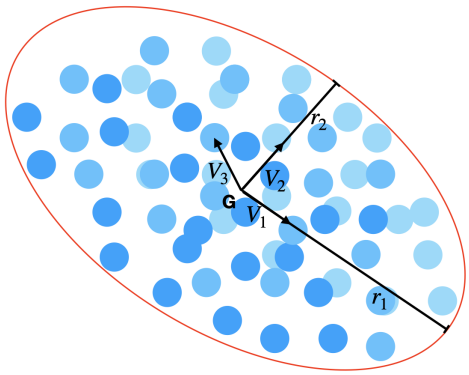

Figure 2: Ellipse shape representing the first crack increment build from a cluster of points having reached the critical value f_{crit}. The ellipse (in red) is defined from its center G corresponding to the barycenter of the broken points, so that it contains all the projections on its surface of the considered points (in blue).

initiation, a more cost effective solution which leads to a more realistic first crack increment is proposed for crack initiation in 3D.

3.2.1. Crack initiation

In 3D. The geometrical approach proposed in this paper consist in approximating the first crack increment for 3D cases by an elliptical surface. This surface is defined as the ellipse shape containing the orthogonal projection of the positions of the broken integration points (*i.e.* points having reached the critical value f_{crit}), see figure 2.

In practice, the center of the ellipse is classically chosen to be the barycenter of the broken points. The plane of the elliptical shape is obtained thanks to the Singular Value Decomposition (SVD) theory [47]. According to this approach, if the coordinates of the considered points are stored in a matrix $\boldsymbol{M}_{\text{coord}} \in \mathcal{R}^{3\times N_{\text{broken}}}$, where N_{broken} is the number of broken points; then this matrix can be decomposed

as follows:

$$\boldsymbol{M}_{\text{coord}} = \boldsymbol{V}.\boldsymbol{\Sigma}.\boldsymbol{W}^t \tag{1}$$

where $\boldsymbol{V} \in \mathbb{R}^{3\times 3}$ and $\boldsymbol{W} \in \mathbb{R}^{N_{\text{broken}}\times N_{\text{broken}}}$ are orthogonal matrices, and $\boldsymbol{\Sigma}$ is the matrix with diagonal coefficients corresponding to the eigenvalue in ascending order (so that it is uniquely defined). Then, the columns of the matrix $\boldsymbol{V}$, respectively $\vec{V_1}$, $\vec{V_2}$, and $\vec{V_3}$, represent the preponderant vectors describing the cluster of broken points. In particular, the plane of the ellipse is defined by $(G, \vec{V_1}, \vec{V_2})$, as illustrated in figure 2. Finally, the radii of the ellipse denoted r_1 and r_2 are chosen so that the ellipse contains all the projections of the broken points on the ellipse plane. For that purpose, it is useful to consider the matrix $\boldsymbol{M}^*_{\text{coord}} = \boldsymbol{\Sigma}.\boldsymbol{W}^t$ which contains the coordinates of each broken point in the new coordinate system $(G, \vec{V_1}, \vec{V_2}, \vec{V_3})$. The radii of the ellipse can then simply be defined by the following:

— for the largest radius: $r_1 = \max_i(|\boldsymbol{M}^*_{\text{coord}}[0, i]|)$ for $i \in [0, N_{\text{broken}}[$;

— and for the smallest radius: $r_2 = \max_i(|\boldsymbol{M}^*_{\text{coord}}[1, i]|)$ for $i \in [0, N_{\text{broken}}[$.

In the case of simple symmetrical boundary conditions (as in section 5.4), the boundary conditions information is conveyed to the initiation algorithm so that the matrix $\boldsymbol{M}_{\text{coord}}$ comprises the coordinates of the damaged points as if determined from the entire reconstructed structure.

Let us underline that, if experimental observation do not corroborate an elliptical planar shape, then the size of the first crack increment should be chosen relatively small. Crack propagation in the following increments should then enable to retrieve the proper shape. Otherwise, combining the determination of

the first crack increment by the Marching Ridges method and a shape optimization procedure would be a more versatile but expensive option.

In 2D. For 2D cases, the Marching Ridges Algorithm provides an efficient and sufficiently cost efficient approach to determine the first crack increment. Its principle is recalled in the next section.

In case of multiple cracks. Several crack initiation sites can be easily defined simultaneously by distinguishing sufficiently damaged areas and considering each area independently. To define these areas, it is possible to use the iso-contour corresponding to a sufficiently high limit value of the considered scalar field.

3.2.2. Crack propagation using the Marching Ridges Algorithm

Principle in 2D. As with any crack path tracking algorithm considering a scalar field, the crack is assumed to appear where the field representing material degradation is maximum, *i.e.* on the ridge of the field. The aim is thus to approximate the crack increments by line segments along this ridge. In the case of the Marching Ridges algorithm, the idea in 2D is to start from a point on the ridge (see below for the selection of this point) and to find incrementally the next points on the ridge of the considered field (here f_t).

As usual with crack path tracking algorithm considering a scalar field, the first step is a smoothing operation performed on the considered scalar field f_t. Following [23, 24], this is done using the super–convergent patch recovery (SPR) technique proposed by Zienkiewicz and Zhu [44]. The general idea is to build, from the initial field computed at the integration points, a smoother field that is defined at the nodes to benefit from the higher order of the displacement interpolation functions. The nodal values of the smoothed field are obtained by

approximating the initial field by a second order polynomial function based on the values at super-convergent points in patches of elements around the vertex nodes. For mid-segments nodes belonging to several patches, an average value is computed. Using these nodal values and the same interpolation functions as for the displacements, the evaluation of the smoothed degradation variable f_t^* or its spatial gradient at any point is straightforward.

Then, it is necessary to define a starting point x_0: in 2D, a simple choice is to consider the maximum point of the scalar field in the considered area for crack initiation and the current crack front for crack propagation. This point can then serve as the center of a polar grid used to evaluate the projection of the spatial gradient of the considered field f_t^* onto the tangential vector $\vec{e}_\theta$ at an evaluation radius R and for a finite number of angles θ separated by the angular accuracy $\Delta\theta$. The next points on the ridge then correspond, schematically, to the points (R, θ) for which the derivative of f_t^* with respect to θ was positive (i.e for $\theta - \Delta\theta/2$) and becomes negative (i.e for $\theta + \Delta\theta/2$):

$$\begin{cases} \vec{e}_\theta(\theta - \Delta\theta/2).\nabla f_t^*(x_0 + R\vec{e}_r(\theta - \Delta\theta/2)) > 0 \\ \vec{e}_\theta(\theta + \Delta\theta/2).\nabla f_t^*(x_0 + R\vec{e}_r(\theta + \Delta\theta/2)) < 0 \end{cases} \tag{2}$$

Adaption to 3D for crack propagation. In [23, 24], a simple method to adapt this planar search for 3D crack propagation was proposed. It consists of performing the 2D search in orthogonal planes to the current crack front. In practice, the current crack front is a line that a finite number of segments can approximate. Remark that this discretization can be completely independent of the FE discretization: *e.g.*, in this work, the crack front line is discretized into segments of length equal to the evaluation radius R. For each segment, defining an orthogonal plane for the 2D search is straightforward. For increased

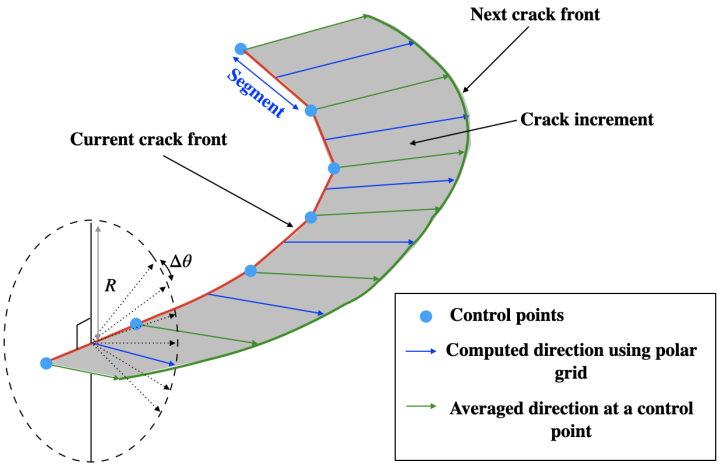

Figure 3: Use of the marching ridges algorithm for 3D structures with 2D polar grid search in planes orthogonal to the current crack front segments, figure a), as proposed in [24]).

robustness, several parallel planes can be defined for one segment to be able to average the resulting direction(s), especially for large segments. The starting point x_0 is then the intersection of the considered plane with the current crack front line. For each segment, the Marching Ridges algorithm provides a direction, or a set of directions in case of crack branching (see figure 3). In case there are several directions for each segment, theses directions are first divided into groups of consistent directions along the whole front based on their relative difference between adjacent segments and the imposed angular precision $\Delta\theta$. Each group of directions is associated with a branch and the branches are then considered independently. For each branch, an average direction (or a set of average directions) is computed for each point connecting two segments using the consistent directions associated with the segments sharing this node. This 3D adaption method is quite generic and can be used with any crack path tracking algorithm developed for 2D cases.

A major difference in this work compared to [23, 24], is that the crack increments do not have the same length for all the segments. Discretizing the current crack front in 3D broadens the methodology's scope. Indeed, for each point between two segments, the propagation length along the average direction is given by the distance to the iso-value $f_t = f_{crit}$. Each point of the current front is then associated to a new end point that serves as control point to build a Bezier curve of degree 2. This Bezier curve ultimately defines the crack increment. As material degradation progresses, the iso-line $f_t = f_{\text{crit}}$ usually gets further from the crack front, thus increasing the size of the crack increment until the insertion criterion allows the insertion of the considered branch.

3.3. Insertion criterion

An insertion criterion determines whether a crack increment is ready to be inserted into the mesh based on the local fields.

3.3.1. In 2D

In the case of 2D simulations, the insertion criterion can be easily defined since the crack increment is a line segment (for both initiation and propagation), especially when inserting crack increments of constant length. It then suffices, as proposed in [23, 24], to evaluate the considered material degradation related field f_t and to allow crack insertion when it exceeds the critical value f_{crit} along the entire crack increment.

The main challenge is then to define an appropriate crack increment size. The aim is then to avoid too frequent remeshing if the crack increment is too small or delayed insertion resulting in stretched elements near the crack front if the crack increment is too large. Following [23, 24], the crack increment length Δa is

here built as a multiple of the localization bandwidth l_b: $\Delta a = m_b \times l_b$, with m_b a multiplication factor that can be tuned (a study on the effect of the crack increment length Δa on the crack path is presented in section 4.1.2 leading to $m_b \approx 4$).

For 3D structures, the insertion criterion has to be more elaborate since the crack can be represented by a complex surface.

3.3.2. For crack initiation in 3D

For crack initiation in 3D, a minimal size of the elliptical crack surface should be determined in order to avoid inserting too small increments into the mesh. In order to be as consistent as possible with the criterion proposed for 2D cases, the authors here propose to proceed to insertion only if both radii of the ellipse (build to contain all the projections of the points with $f_t \geq f_{\text{crit}}$) are greater than the value $\Delta a = m_b \times l_b$.

3.3.3. For crack propagation in 3D

Considering constant crack length increments had provided satisfactory results in [24]. However, such a progression with constant crack increments corresponds to an isotropic propagation of the current crack front. When this is not the case and the crack increment does not have a simple geometrical shape, a new insertion criterion has to be defined. The authors propose here to compare the area of the crack increment, denoted A_{real}, with the area considered when using uniform crack length increments, denoted A_{unif} and to allow insertion only when the area A_{real} is greater than A_{unif} (see figure 4).

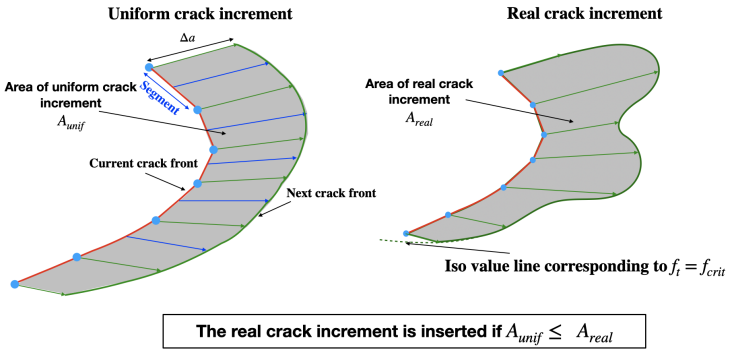

Figure 4: The proposed insertion criterion for crack propagation in 3D structures compares the area of the crack increment with constant length for each segment, A_{unif}, and the area obtained with different lengths, A_{real}: insertion is allowed only when $A_{\text{real}} \geq A_{\text{unif}}$.

3.4. Mesh adaption

Mesh adaption is a natural choice to ensure that the aspect ratios of the elements stay correct throughout the simulations within a finite strain framework. That is why mesh adaption is performed on the current configuration at a given frequency $\Delta t_{\text{remeshing}}$ set by the user, even before serving to represent the discontinuity.

3.4.1. Representation of the discontinuity

Insertion of the discrete crack into the volumetric mesh here relies on a cutting operation of the external boundary of the mesh by the crack surface. A robust cutting algorithm introduced in [25] is used to perform this operation. Note that the same cutting algorithm is used to perform discrete crack propagation in fatigue problems [48, 49]. This cutting algorithm produces a surface mesh incorporating both the outer surface of the mesh of the structure and the crack surface. Then, an additional refinement operation, using *meshGems* [45], is performed in order to

fill in the volume of the created surface mesh and generate a suitable mesh with acceptable element quality and adapted discretization thanks to local refinement.

3.4.2. Local refinement of Active Process Zones

Local refinement is used throughout the simulation in order to achieve a compromise between accuracy and cost. The idea is to use coarser elements in the areas where damage does not significantly evolve and to only refine the mesh in *Active Process Zones* (APZ). Inside the APZ, the minimal element size h_{min} necessary for the convergence of the mesh (as defined in [10]) is imposed. Outside the APZ, the sizes of the elements are linearly interpolated between the minimal and maximal sizes, respectively h_{min} and h_{max}, according to the distance of the considered element from the APZ.

The APZ is defined during crack propagation by a circle in 2D, centered on the farthest point from the crack front, taken along the last crack increment direction, where the considered scalar field f_t reaches $f_{\text{crit}}/m_{\text{APZ}}$, where m_{APZ} is a user defined constant greater than or equal to 2. The radius of the APZ, L_{APZ}, is then the distance between this point and the crack front (see figure 5-b). In 3D, the APZ is the cylinder revolving around a 1D center line approximating the positions of the points reaching the value $f_{\text{crit}}/m_{\text{APZ}}$ ahead of the crack front line. The APZ then lies between the center line and the crack front.

Note that is is also possible to define APZ to be refined before crack initiation to properly describe the early stages of the damaging process (see figure 5-a). In this case, the APZ is defined by a circle in 2D or a sphere in 3D, centered on the potential locations of crack initiation and the radius of the circle L_{APZ} is the maximum distance between two points reaching f_{crit} and $f_{\text{crit}}/2$ respectively (or $f_{\text{crit}}/m_{\text{APZ}}$ with $m_{\text{APZ}} \geq 2$ to be able to consider a larger area). In the

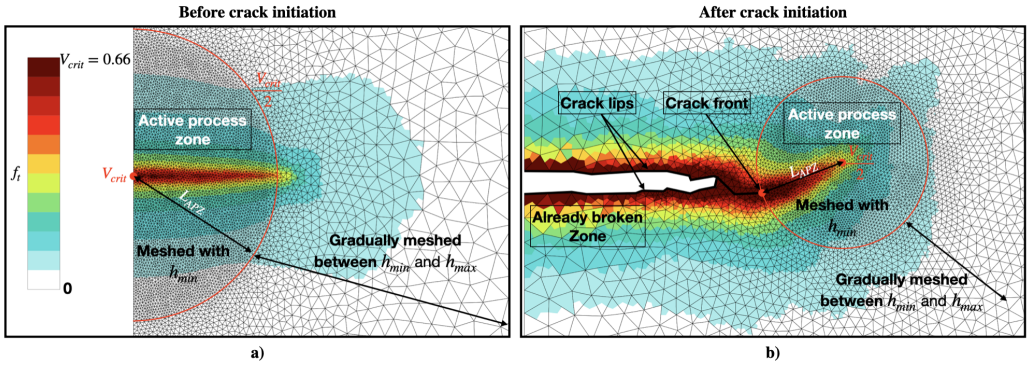

Figure 5: Automatic detection of the Active Process Zone (APZ) for the remeshing procedure: the center and radius definitions change (a) before and (b) after crack initiation. Using this procedure, only the Active Process Zone ahead of the crack front is finely meshed. The mesh used in areas already crossed by a crack becomes coarser depending on the distance to the crack front.

present case, the potential locations of crack initiation are simply based on prior knowledge to already have a fine mesh when the constitutive behavior becomes nonlinear. However, it is also possible to obtain similar results thanks to an automatic adaptive mesh procedure based on error estimation as in [23], with the right choice of parameters for the error estimator and the refinement criterion.

3.5. Transfer operator

In order to resume the simulation after each discretization change, it is necessary to transfer the data stored at the nodes and integration points from the old mesh to the new mesh.

3.5.1. Nodal data transfer operator

The procedure for transferring the nodal variables is standard: each node of the new mesh is located in an element of the old mesh, and then the new nodal value is calculated using the element's shape functions. In the present case, since

the remeshing is performed on the current configuration, the displacement vector $\vec{u}$ is set to $\vec{0}$ on the new mesh, so no transfer is needed for the displacement field. However, since the considered model is based on an implicit gradient formulation, the nonlocal nodal variable are transferred using the described method.

3.5.2. Integration points data transfer operator

For the state variables stored at the integration points, the nearest integration point transfer technique is used [46]. This technique has been chosen to preserve the high gradients of the localized variables and limit the transfer costs, since no smoothing operation is used. Note that a prerequisite to using this technique is that the meshes do not change significantly before and after remeshing. This is the case with the proposed mesh adaption procedure thanks to a regular refinement (due to the mesh adaption frequency $\Delta t_{\text{remeshing}}$ or to the insertion of sufficiently small crack increments) of the APZ which moves progressively as the crack advances, with a gradually evolving mesh size outside the APZ.

3.6. Reequilbrium using a relaxation step

Independent transfer operations on the nodal and integration point variables create unavoidable errors: in particular, neither the global equilibrium equations nor the local constitutive equations are satisfied. The transferred strains are also not consistent with the nodal displacements. These inconsistencies in the transferred fields degrade the convergence rate after remeshing and thus may lead to a large number of increments if a load increment division procedure [38] is used. Too large errors can even lead to a divergence of the resolution algorithm. In this paper, the authors propose a novel re-equilibrium method based on the elastic balancing step introduced in [40].

The idea behind Mediavilla's method is to retrieve equilibrium thanks to an additional step with frozen boundary conditions during which there should be no evolution of state variables like plasticity and damage. This balancing step then consists in solving the mechanical problem using the transferred nodal and integration data while considering an elastic behavior. However, in presence of damage and crack insertion for viscous material, even with this balancing step, based on the authors' experience, degradation of convergence rate and risk of divergence are still problematic. Part of the problem may come from plastic strain and damage variables being kept constant.

To overcome these problems, the authors propose to adapt this re-equilibrium procedure for viscous material: the boundary conditions are also frozen for a non-null time increment Δt_{reeq}, but this increment is divided into several sub-increments during which the mechanical problem is solved considering the usual material behavior, as opposed to the elastic behavior used in [40]. This procedure can be interpreted as a viscous relaxation of the material. Plasticity and damage are then free to evolve. However, this evolution should be rather negligible due to the fixed boundary conditions and the specific choice of a small time increment for the re-equilibrium procedure. Indeed, the re-equilibrium time increment Δt_{reeq} is taken as a fraction (1/10, 1/100, or 1/1000) of the time increment required for convergence during the ductile failure process. The first sub-increments are also taken very small but the following ones rapidly increase, until the imposed time Δt_{reeq} has elapsed. On average, it is observed, for the considered model, that the number of sub-increments during the re-equilibrium stage following a crack increment insertion is about 8. After this re-equilibrium step, the usual boundary conditions are considered again, and the usual convergence rate should

be retrieved or only slightly diminished.

3.7. Summary of the parameters of the continuous–discontinuous procedure

Table 1 lists the parameters of the continuous–discontinuous procedure used for all the applications presented in this paper. Some of the parameters are given as multiples of the localization bandwidth l_b. This is the case for the minimum element size $h_{\min}$, so that there are enough elements to discretize the width of the localization band. This width is strongly linked to the characteristic length of the non local model l_c and depends, for a given characteristic length, on the type of specimen. Indeed, proportional relations were found in [10] for the axisymmetric ($l_b = 2.13 \times l_c$) and the plane strain specimens ($l_b = 1.86 \times l_c$). Ideally, the localization bandwidth l_b should be identified from experimental tests, either directly by local measures or indirectly by identifying the characteristic length l_c from the global response first. In the absence of local measures, the second option was chosen in [10] and the same material characteristics, presented in Table A.2, are considered in this paper, unless specified otherwise.

4. Evaluation of robustness and cost efficiency

In this section, the robustness and cost efficiency of the proposed continuous-discontinuous approach is illustrated on non local 2D simulations of an axisymmetric tensile test for different mesh sizes and different crack increment sizes Δa. The dimensions of the specimen as well as the boundary conditions are shown in figure 6-a. This specimen corresponds to one of the experimental results in [50]. The same experimental test was used in literature as benchmark simulation [10, 15, 51, 52].

Table 1: The parameters of the continuous-discontinuous procedure. The notation l_b designates the localization bandwidth that can be measured following the methodology described in [10].

Remeshing parameters		
Minimal element size	h_{min}	$l_b/2$
Size of APZ	m_{APZ}	2
Remeshing frequency	$\Delta t_{\text{remeshing}}$	adjustable
Marching ridges algorithm		
Evaluation radius	R	$4 \times l_b$
Angular precision	$\Delta\theta$	5°
Insertion criterion		
Critical value for insertion	f_{crit}	$0.95/q_1 = 0.63$
Crack increment length	Δa	$4 \times l_b$
Re-equilibrium time increment	Δt_{reeq}	10^{-4}s

4.1. Robustness

4.1.1. Mesh size independence

In order to illustrate the robustness of the continuous–discontinuous approach, results obtained with different mesh sizes for the same structure are compared. The only restriction in the choice of the considered mesh sizes is that they should lead to converged results. For regularized problems, converged results can only be obtained if the localization band is discretized with several elements. Consequently, to consider a valid choice of minimal mesh element sizes, it is necessary to first determine the width of the localization band l_b. In the present case, it is possible to refer to [10] and the linear relation found between the characteristic length l_c and the bandwidth size l_b^{axi} identified for this axisymmetric

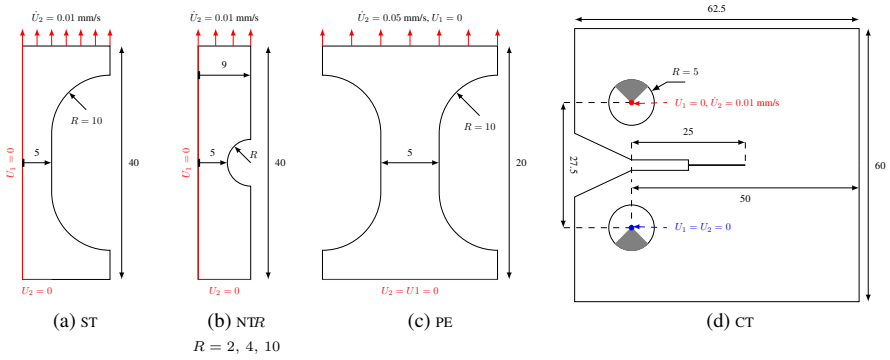

Figure 6: Geometries of the various specimens and boundary conditions. Dimensions in mm.

test:

$$l_b^{axi} = 2.13 \times l_c \tag{3}$$

For the considered model, there are two characteristic lengths. The smallest one (*i.e.* $l_\kappa = 20\mu$m) being the more restrictive, it is the one considered to evaluate the bandwidth: $l_b = 42.6\mu$m. Consequently, meshes with minimum size $h_{\text{min}} \in \{10, 20, 40\}\mu$m are considered. For comparison purposes, a simulation with a very fine fixed mesh with $N_h = 180$ elements in the minimal cross section and an initial element aspect ratio equal to $6:1$, without crack insertion, is also considered.

In Figure 7, the evolution of the engineering stress is displayed as a function of the diameter reduction for all the considered meshes and the total porosity f_t for each mesh size at total failure is also shown.

For all the adapted meshes with minimal element size $h_{\text{min}} \leq 40\mu\text{m} \leq l_b$ enabling mesh convergence, the global response is very similar to the simulation using a very fine mesh ($N_h = 180$) without crack insertion, which is assumed to provide converged results. A cup–cone crack path is obtained for all the considered meshes. The proposed procedure is thus rather robust to the choice of the mesh size while enabling to capture a more realistic crack lip opening

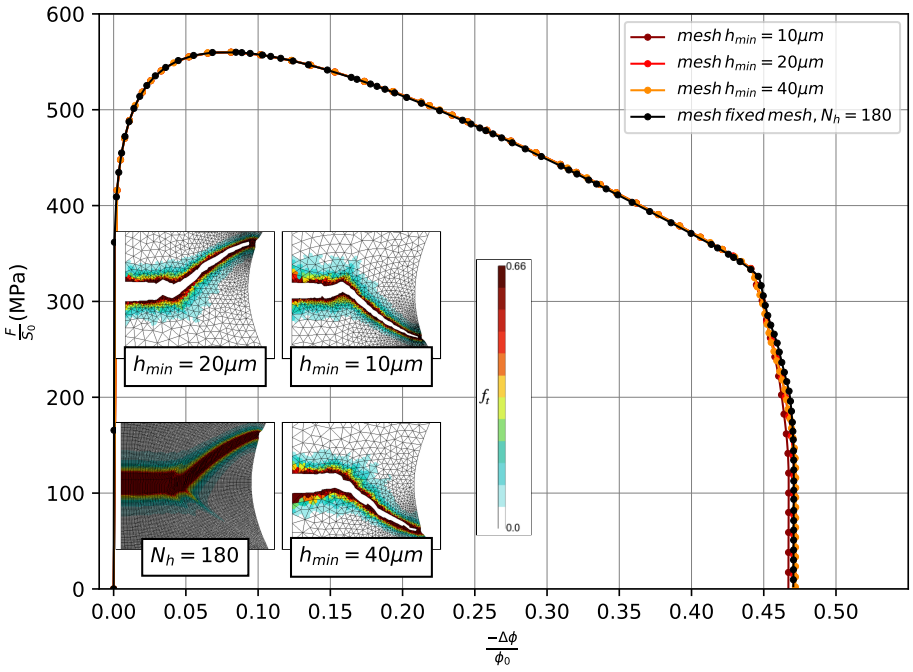

Figure 7: Evolution of the engineering stress as a function of the diameter reduction $-\Delta\phi/\phi_0$ for different minimal mesh sizes obtained when simulating a tensile test on an axisymmetric specimen, and the corresponding porosity map near complete failure.

compared to the simulation without crack insertion. Indeed, for the simulation without mesh adaption, the crack is represented in a smeared manner and the position of the crack lips or crack front is simply not defined.

4.1.2. Effect of the crack increment size

The crack increment length Δa is an important parameter of the proposed procedure because it affects both the discretization of the crack path and the number of mesh adaptions (through the insertion criterion). On the one hand, its choice is guided by considerations similar to the ones guiding the choice of the element size for any finite element computation, *i.e.* it should be:

1. Small enough to enable a proper discretization, in this case, of the crack path;
2. Large enough in order to minimize computational cost, in particular to limit the cost associated with a change of discretization by limiting the number of crack insertions. Note that in the present case, choosing large increments also means less transfer-related errors, whereas for standard finite element computations, larger elements usually lead to more discretization error.

On the other hand, this choice should also be guided by an additional constraint when considering a scalar variable presenting a plateau instead of a sharp ridge: the crack increment length should not be smaller than plateau width; otherwise, the crack path may zigzag. This is the case here since the porosity variable ends up saturating locally due to the choice of regularization through an implicit gradient formulation. That is why only crack increment lengths larger than the localization bandwidth are considered in this study.

Three simulations with the same minimum element size $h_{\min} = 20\mu$m but different crack increment lengths, *i.e.* $\Delta a \in \{80, 160, 240\}\mu$m, are compared in the following. As shown in figure 8, the evolution of the engineering stress as a function of the diameter reduction is the same for the three crack increment lengths. Thus, the global response is quite robust to the choice of the crack increment length. This also means that it is necessary to use different criteria to choose an appropriate crack increment length. By looking at the different contours of total porosity at complete failure in figure 8, one can see that for the largest increment, *i.e.*, $\Delta a = 240\mu m$, the crack path is not entirely smooth, which can be explained by excessive stretching of the elements near the crack front due to delayed insertion. Smaller sizes should thus be considered. The

choices $\Delta a = 160\mu$m and $\Delta a = 80\mu$m lead to rather similar crack paths. However, in the first case, only 20 mesh adaptions are necessary to obtain the complete propagation compared to the 38 mesh adaptions needed for the smallest crack increment length. In order to minimize computational costs, the value $\Delta a = 160\mu$m should be preferred. This crack increment length corresponds to four times the evaluated localization bandwidth (*i.e.* $\Delta a = 4 \times l_b$), which is the order of magnitude recommended by the authors.

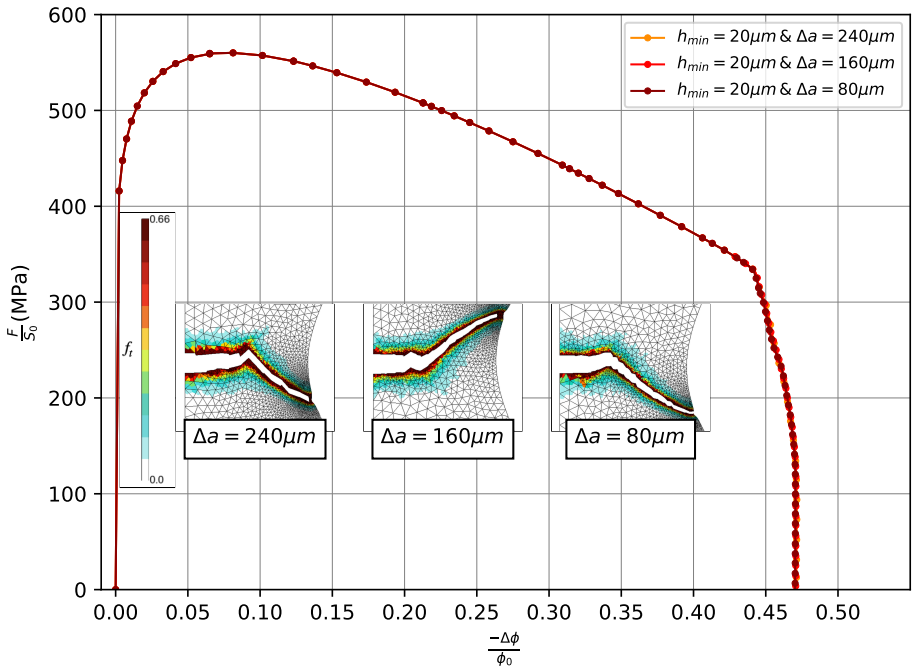

Figure 8: Evolution of the engineering stress as a function of the diameter reduction $-\Delta\phi_0/\phi$ for different crack increment lengths Δa, using the proposed continuous–discontinuous method, in the case of the axisymmetric specimen, and the corresponding porosity map near complete failure.

4.2. Cost efficiency

4.2.1. Gain from refining only the Active Process Zones

In this section, the gain from refining only the Active Process Zone is evaluated. For that purposes, the three following approaches are compared in terms of the number of nodes:

1. The proposed continuous–discontinuous procedure where refinement is used only for the Active Process Zone;
2. An approach with mesh refinement without coarsening fully cracked zones;
3. A simulation with a fixed mesh (*i.e.* without any mesh adaption) using rectangular quadratic elements with $239\,123$ nodes. This last case is meant to be representative of a situation where the exact crack path is not known *a priori*. In that case, the minimum element size to achieve convergence is used in the entire zone where the crack is assumed to propagate.

For both cases with mesh adaption, triangular elements are used with a minimum element size $h_{min} = 20\mu$m. Note that, according to the conclusions of section 4.1 and although not shown in this paper, all three approaches lead to similar global responses and identical crack paths.

In Figure 9, the evolution of the total number of nodes, as the meshes are adapted, is given for all the considered approaches. Note that the smallest number of nodes is obtained with the proposed procedure: about three times smaller at the end of the simulations than the mesh adaption procedure without coarsening and 13 times smaller than the fixed mesh. Besides, with the proposed approach, the total number of nodes is approximately the same for all remeshing steps. In other words, the total number of nodes does not depend on the length of the crack, in contrast with the second procedure without mesh coarsening, for which the

number of nodes steadily increases as the crack propagates. In terms of CPU time, the proposed approach consisting in refining only the Active Process Zones leads to a speed up of 6 compared to the fixed mesh computation[1], although the number of required increments is doubled. This approach is thus very cost effective.

4.2.2. Gain from the re-equilibrium procedure

In this section, in order to evaluate the cost-effectiveness of the re-equilibrium procedure, the computational cost for three simulations are compared:

1. a simulation with the full proposed approach, *i.e.* using the re-equilibrium procedure;
2. a simulation very similar to the proposed approach but without using the re-equilibrium procedure;
3. a simulation with a fixed mesh that does not use remeshing nor crack insertion.

Note that, according to the conclusions of section 4.1 and although not shown in this paper, the global response obtained in all the three studied cases is identical.

Since each iteration involves the update of the local internal variables and the inversion of the global stiffness matrix, which are quite expensive operations, especially with a nonlinear problem, the accumulated number of iterations is an appropriate measure of the computational cost. In figure 10, the evolution of the accumulated number of increments is given as a function of the imposed vertical displacement U_2^d from $U_2^d = 3$ mm. The highest number of time increments is

[1]Both simulations are carried out on a machine (32cpus, 96 Go RAM) using the Mumps solver [53, 54]

obtained for the simulation with mesh adaption without re-equilibrium. Using the re-equilibrium procedure, the total number of increments is approximately divided by two. The lowest number of time increments is obtained for the fixed mesh (*i.e.* without any field transfer): only 690 time increments are needed to obtain total failure. In this case, the discrete crack is not represented, so that transfer is unnecessary. In all cases, the crack propagation phase (*i.e.* after the moment the first integration points reach f_{crit} for the fixed mesh) is accompanied by an increase in the number of increments. It can thus be assumed that, whatever the considered approach, the severity of the nonlinearities associated with the damage evolution during the fracture process is, at least partially, responsible for the difficulties in converging. However, additional difficulties appear when adapting the mesh to insert a crack increment, as the number of increments seems to increase more rapidly as soon as the crack initiates. There is indeed a cost that has to be paid in order to introduce, in the continuous model, a discrete and well-defined crack. However, this cost can be limited thanks to the proposed re-equilibrium procedure. Indeed, the number of time increments is twice smaller than without re-equilibrium.

5. Numerical applications

The purpose of this section is to demonstrate the effectiveness of the proposed continuous–discontinuous approach, and in particular of the new ingredients, on several cases from the literature. The considered cases are selected among the most used specimens for material identification and either lead to non-trivial crack paths (like tensile tests on notched or smooth round bars) or present some difficulty for its simulation (like a tensile test on a CT specimen resulting

in relatively long crack propagation). Numerical applications are presented in various frameworks: 2D axisymmetric, 2D plane strain, and 3D simulations.

5.1. Cup-cone failure for axisymmetric smooth and notched specimens

In this section, more cases presenting a cup–cone failure are tackled: round specimens with different notch radii ($\{2, 4, 10\}mm$) and a smooth round bar are simulated with 2D axisymmetric meshes. Note that the smooth round bar becomes notched-like as soon as necking starts. Figures 6-a and b give a description of the geometries and boundary conditions. The interest in considering several radii is to study the effect of the stress triaxiality ratio on the crack path since triaxiality increases as the notch radius decreases. The results are first compared in terms of evolution of the engineering stress as a function of the diameter reduction $-\Delta\phi/\phi_0$ in figure 11. It appears that ductility decreases with the notch radius. This observation is in agreement with experimental observations [55, 56]. In the same figure, three stages of the simulation are highlighted with numbered arrows for each specimen. Corresponding contours of the total porosity are plotted for each highlighted stage in figure 12. For every specimen, the crack is initiated (stage 1) at the center where stress triaxiality is maximum. Then for all the specimens, a cup–cone crack path is predicted (stage 2). Stage 3 corresponds to full failure. It is interesting to note that the distance from the symmetry axis at which the cup–cone crack path bifurcates increases as the notch radius decreases: this indicates that the location at which the crack bifurcates to form the cup-cone is a function of the triaxiality at the center of the specimen.

5.2. Slant fracture prediction for 2D plane strain tensile tests

In this section, the proposed continuous–discontinuous procedure is applied to predict slant fracture for a plane strain tensile test selected from [50, 57]. The geometry and boundary conditions are presented in figure 6-c. It is interesting in this case to compare the results with a fixed mesh without crack insertion since, contrary to the cup–cone fracture simulations in figure 7, slight differences are found in this case. Note that both discretizations are chosen sufficiently fine in order to have converged results: *i.e.* with a minimum element size of $h_{\min} = 20\mu$m for the triangular meshes generated with the proposed procedure and with $N_h = 180$ rectangular elements in the cross-section for the fixed mesh.

In figure 13, the evolution of the engineering stress is plotted as a function of the thickness reduction $-\Delta e/e_0$ for the simulation using the proposed procedure and the simulation with a fixed mesh. Similar global responses for both simulations are obtained up to the latest stages of the simulation. At this point, the simulation with crack insertion ends up with a slightly larger final thickness reduction. In order to better understand this difference, it is interesting to consider the total porosity contours in the same figure. In both cases, a slant crack path is predicted. However, with the fixed mesh, the slant crack path is symmetric regarding the central vertical axis, whereas with the proposed continuous–discontinuous procedure, an antisymmetric slant crack path first appears before a bifurcation towards another shear band is observed. The occurrence of the crack bifurcation seems to coincide with the deviation of the global curve for the proposed approach from the fixed mesh curve. The difference between the crack paths may then explain the difference in the global responses at the latest stages of the simulation.

Note that this bifurcation of the slant fracture towards another shear band was also reported in the numerical work of Leclerc *et al.* [15] using a different ductile model and a different continuous–discontinuous approach. However, in the work of Leclerc *et al.*, only one-half of the specimen was modeled, which means that the symmetry conditions impose a symmetric crack path regarding the central vertical axis, thus always resulting in a V-shape crack (see also [57]). In the present case, a V-shape crack is also observed for the computation without mesh adaption from a mesh which is symmetrical regarding the central vertical axis, whereas an S-shape crack is obtained when mesh adaption is used and no symmetry conditions are imposed. Let us note that the difference in shape is already present even before crack insertion (see point A in figure 13). The reason for the differences between both crack paths remains unclear, although it can be assumed the symmetry of the mesh for the case without mesh adaption has favored the V-shape. Experimentally, both cases can be observed (e.g. see figure 3-a of [58]).

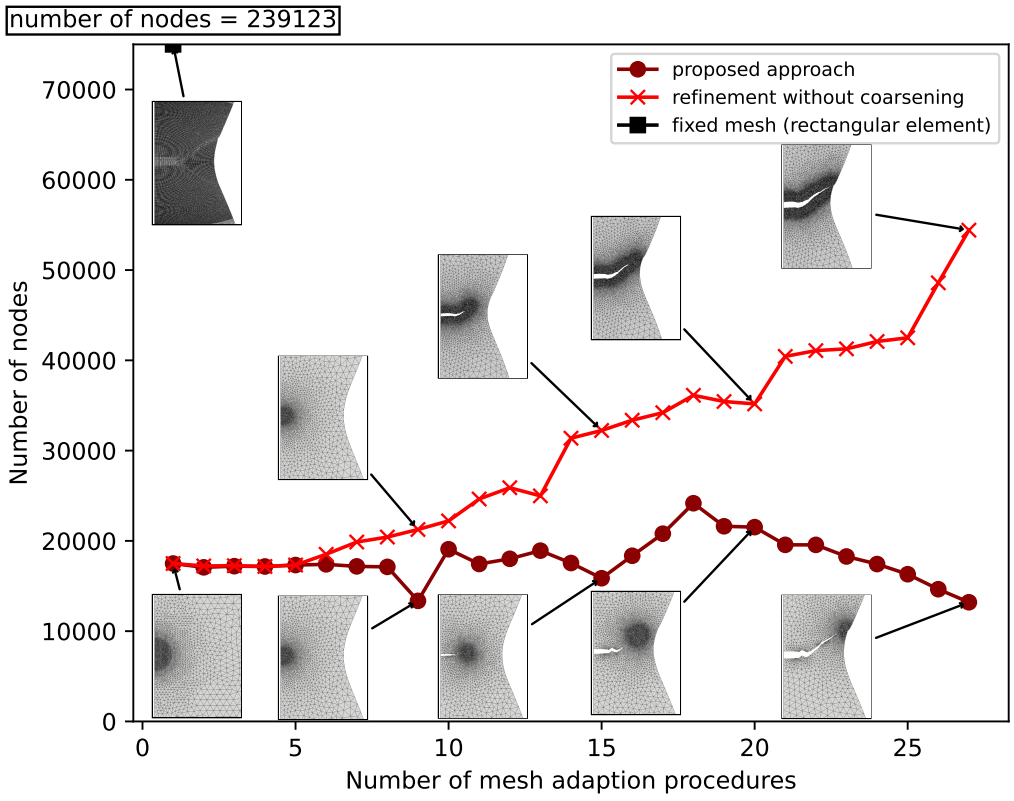

Figure 9: Evolution of the number of nodes as a function of the number of mesh adaption steps with refinement of only the Active Process Zones (in dark red), mesh adaption without coarsening of the cracked zones (in light red) and a fixed mesh (in black). The first approach consistently leads to a smaller and rather constant number of elements.

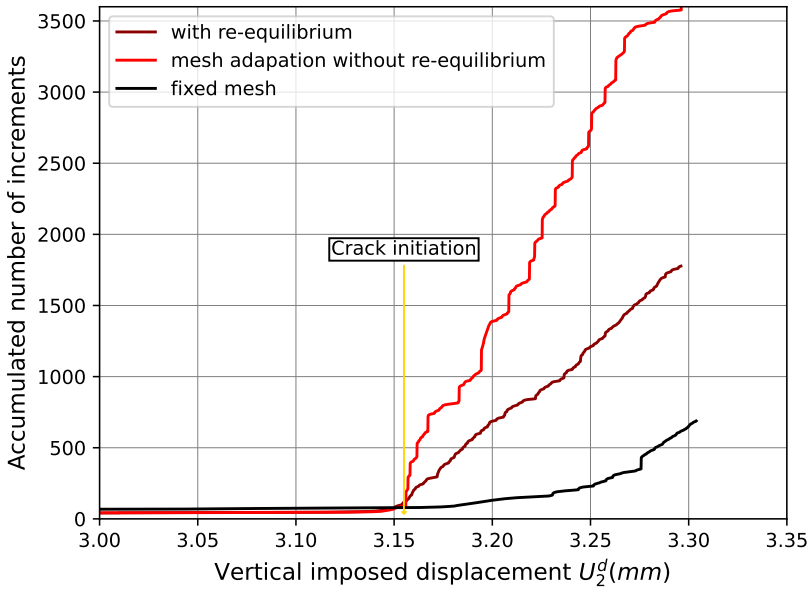

Figure 10: Evolution of the accumulated number of time increments as a function of the imposed vertical displacement for the simulation of the axisymmetric tensile test on a fixed mesh (in black), with mesh adaption but without re-equilibrium (in light red) and with mesh adaption and the proposed re-equilibrium procedure (in dark red).

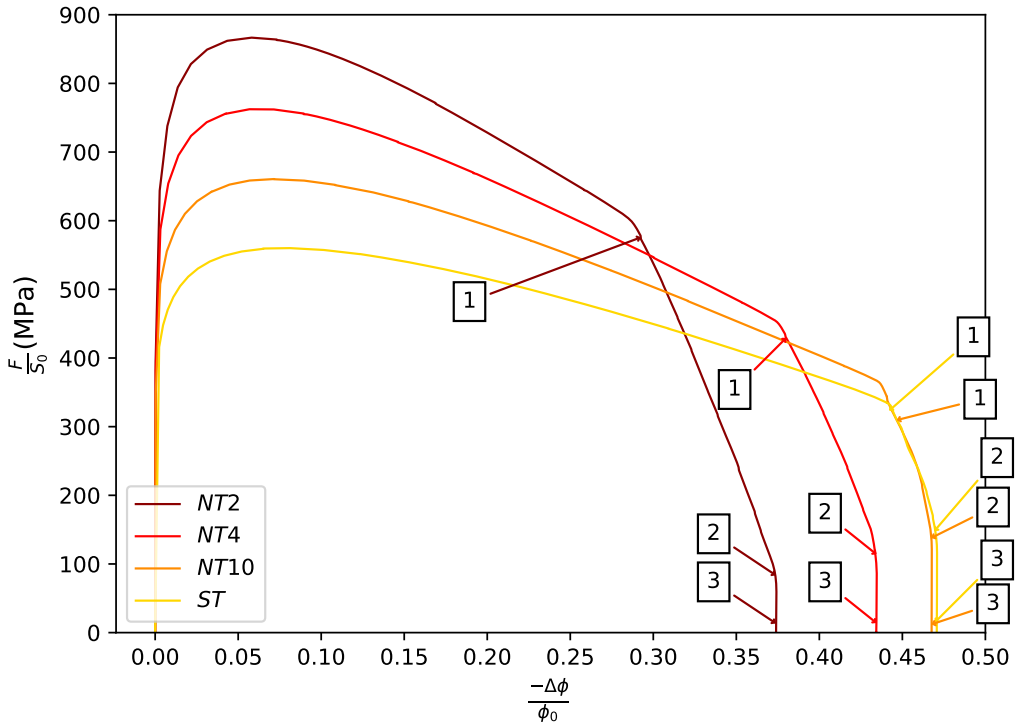

Figure 11: Evolution of the engineering stress as a function of diameter reduction $-\Delta\phi/\phi_0$ for all considered axisymmetric specimens, using the proposed continuous–discontinuous approach. The final diameter reduction decreases with the notch radius. For each global response, three particular instants of the simulation are highlighted with a numbered arrow in order to track damage evolution and crack path in figure 12.

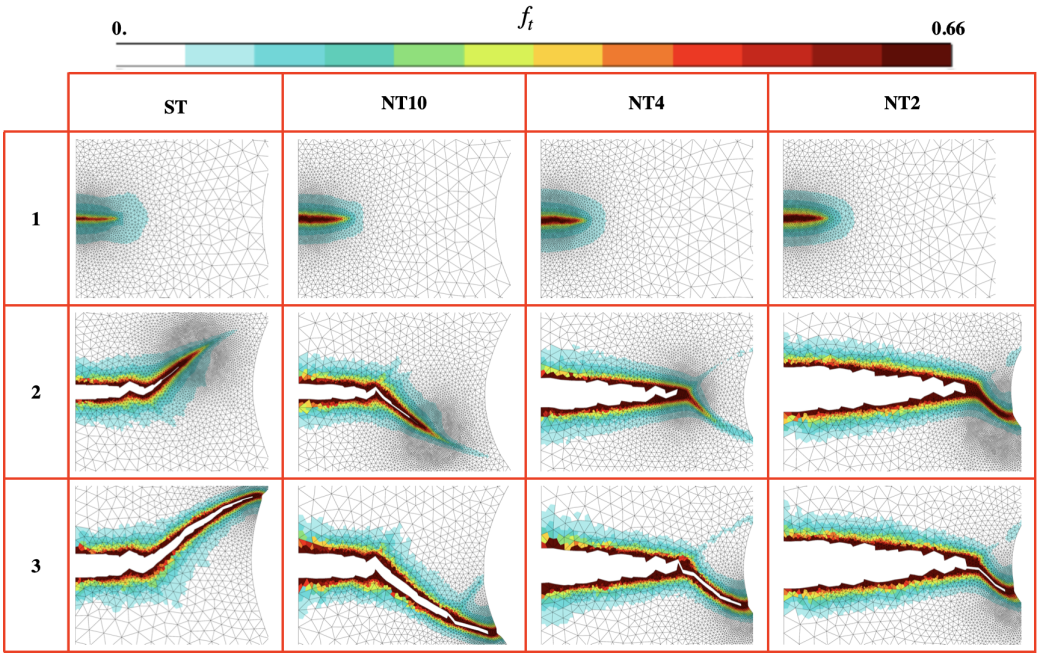

Figure 12: Total porosity f_t contours at the three instants of the simulation highlighted in figure 11, for all the considered axisymmetric specimens. For all the specimens, there is a cup–cone crack path at stage 2. Note that, for the round bar specimen, necking causes the boundary to appear as curved at these advanced stages of material degradation.

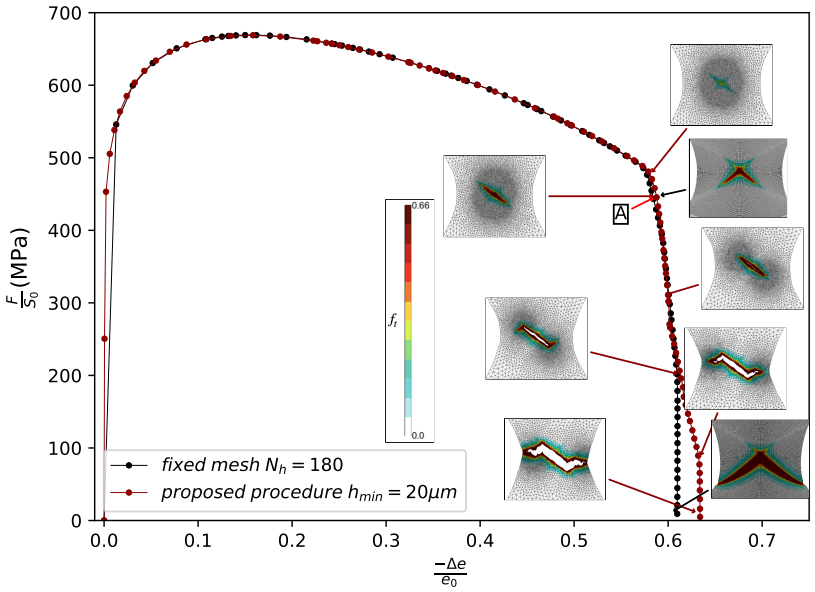

Figure 13: Evolution of the engineering stress as a function of the thickness reduction $-\Delta e/e_0$ of the plane strain specimen for both a simulation with the proposed continuous–discontinuous procedure and a simulation with a fixed mesh. Total porosity is displayed at various times of the simulation using the proposed method, and at total failure for the fixed mesh simulation.

5.3. Blunting and long crack propagation for a 2D plane strain CT test

In this section, a 2D plane strain simulation of a test on a Compact Tension (CT) specimen is used to illustrate the capability of the proposed continuous–discontinuous procedure, and in particular of the mesh adaption procedure limited to the APZ, to predict crack tip blunting before crack initiation and to simulate long crack path propagation. The geometry and boundary conditions can be found in figure 6-d. In the absence of a prior convergence study for that particular geometry, two simulations with minimum element sizes $h_{\min} \in \{20, 40\}\mu$m are performed to verify the mesh convergence.

In figure 14, the evolution of the force per unit thickness is plotted as a function of Crack Mouth Opening Displacement (CMOD) for the two considered meshes. Both curves are identical, which indicates that mesh convergence is achieved. Besides, based on the contours of total porosity in the same figure, it can be seen that before crack initiation (marked with a green cross), crack tip blunting is gradually developing and well captured by the simulation thanks to mesh adaption which enables the preservation of good quality elements near the crack tip. This good representation of crack tip blunting would be more challenging to obtain with a fixed mesh due to stretched elements near the crack tip. Furthermore, thanks to crack insertion into the mesh, a stable and relatively long crack propagation until total failure is obtained with, all along, a well-represented crack opening and good quality elements even in the presence of large strains near the crack tip. Meanwhile, coarsening of the non-active process zones behind the crack tip enables to keep the number of nodes approximately constant throughout the crack propagation process and thus to limit computational cost.

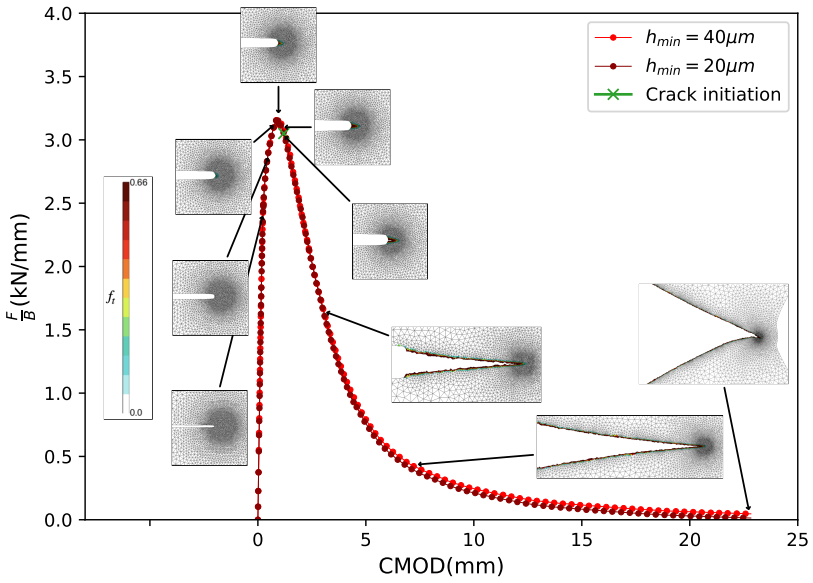

Figure 14: Evolution of the force per unit thickness (F/B) as a function of the Crack Mouth Opening Displacement (CMOD) for two meshes with different minimum element sizes, $h_{\min} \in \{20, 40\}\mu$m, of a CT specimen. Contours of the total porosity f_t are displayed at different steps of the simulation.

5.4. 3D simulation of cup–cone failure

In this section, a 3D simulation of a cup–cone failure on a simple round bar (without any notch) is presented to illustrate the efficiency of the proposed ingredients that are specific to 3D, *i.e.* the proposed geometrical approach to approximate the very first crack increment as an elliptical crack surface, and the proposed insertion criterion based on the area of the crack increment. The considered initial mesh is presented in figure 16-a: only a quarter of the specimen is simulated to reduce the computational costs. Indeed, despite the gain offered by the new ingredients for the post-processing operations related to crack increment insertion (see 4.2), 3D simulations are still quite expensive due to the integration

of the constitutive behavior for a very large number of elements and the resolution of the linearized mechanical problem. For the same reason, larger elements are considered here, with $h_{\min} = 80\mu$m (*i.e.* four times larger than for the previously presented 2D simulations of cup–cone in section 5.1). Consequently, larger minimum characteristic lengths are also used to have a sufficient number of elements to discretize the localization band (here $l_\kappa = l_\omega = 40\mu$m). The results are confronted with the ones obtained performing, on the one hand, a 2D axisymmetric simulation using the proposed continuous–discontinuous procedure and a finer mesh ($h_{\min} = 20\mu m$) and on the other hand, a 2D axisymmetric simulation with a fixed mesh with $N_h = 180$ rectangular elements discretizing the cross-section.

In figure 15, the evolution of the engineering stress is plotted as a function of the diameter reduction $-\Delta\phi/\phi_0$ for the three considered simulations. The global responses are very similar, which tends to validate the results of the 3D simulation. Contours of the total porosity f_t are also displayed at different steps for the 3D simulation to illustrate the cup–cone crack path. The final cup–cone fracture surface obtained with the 3D simulation is shown in figure 16-b. Let us note that the procedure enables to reach complete failure of the specimen which is broken in two pieces. It is clear that the crack lips are particularly well described and smooth thanks to the proposed continuous–discontinuous procedure. This is an advantage of the discrete crack determination, which requires the use of a crack path tracking algorithm. Note that using the proposed procedure, there is no material loss compared to procedures using element erosion prior to mesh adaption. Besides, the cup–cone fracture surface obtained with the 3D simulation is in good qualitative agreement with the experimental results of Besson et al. [57]

(also reproduced in [11]).

6. Conclusion

In this paper, some new contributions were proposed to enable a robust and cost–efficient transition from a continuous model evaluating local material degradation to a model representing propagation of a discrete crack. These contributions have been evaluated using the nonlocal GTN model with two characteristic lengths proposed in [10] thanks to complex crack path simulations (*i.e.* either non-trivial crack paths or challenging simulations with large strains and long crack propagation).

Two of these contributions mainly aimed at limiting the computational cost. On the one hand, a new procedure was proposed to facilitate the return to equilibrium and to improve the convergence rate after remeshing. The authors have shown that this re-equilibrium procedure limits the number of increments during crack propagation, which contributes to the cost-efficiency of the method. On the other hand, a pragmatic remeshing procedure was proposed to refine only the Active Process Zones. This proposition has a double advantage: (i) the degradation phenomena leading to complete failure are well described, (ii) the number of elements (and thus the computational cost) remains approximately constant.

Two more contributions, on rarely tackled subjects, are proposed specifically for simulations in 3D. The first one deals with crack initiation entirely inside the structure: a simple geometrical crack initiation methodology based on SVD analysis of the coordinates of broken points was proposed to generate an elliptical-shaped first crack increment. This solution offers a gain in computational cost

compared to the method of [23, 24]. Finally, the last contribution was a new insertion criterion to select both the most appropriate time to insert a given crack increment and the crack increment surface.

The robustness and cost efficiency of the proposed continuous–discontinuous procedure have been validated in several ways with, whenever possible, comparisons with simulations on a fixed very fine mesh. Different minimum element sizes were tested in order to show the insensitivity of the procedure to the mesh size. Several crack increment lengths were considered in order to illustrate the insensitivity of the global response and to propose guidelines for the choice of the optimal crack increment length. In all cases, it was verified that the simulated crack surfaces were, in comparison with numerical simulations or experimental observations from the literature, in qualitatively good agreement.

These new features enabled to successfully simulate several tension tests of specimens used to identify material parameters with both plane strain and axisymmetric elements and finally the challenging case of a cup–cone failure in 3D.

Three among the four proposed ingredients are quite generic and could be used with a different discontinuity representation, *i.e.* with XFEM or even to perform controlled element erosion: (i) the simple geometrical approach to approximate the first crack increment by an elliptical crack shape in 3D meshes, (ii) the new 3D insertion criterion and (iii) the re-equilibrium procedure.

Note that, although the proposed contributions enable to significantly reduce the cost associated with cracking insertion, the resolution of the mechanical problem remains expensive in 3D. It would then be interesting to combine this

approach with parallel computing. This could be particularly beneficial in the case where several cracks appear in different areas to perform the post-processing operations related to crack detection, insertion, and propagation in each area independently.

Appendix A. Material models and their framework

The nonlocal model used in this study is the implicit gradient GTN model with two characteristic lengths presented in [10] where its implementation is detailed. The model is briefly recalled in the following.

Appendix A.1. Material model

One assumes an additive decomposition of the strain tensor ($\boldsymbol{\varepsilon}$) into an elastic ($\boldsymbol{\varepsilon}_e$) and a plastic ($\boldsymbol{\varepsilon}_p$) part. The elastic strain tensor and the stress tensor are related using Hooke's law:

$$\boldsymbol{\sigma} = \mathbb{E} : \boldsymbol{\varepsilon}_e \tag{A.1}$$

where $\mathbb{E}$ is the fourth order elasticity tensor. Work hardening is assumed to be isotropic, and the flow stress of the sound material ($R(\kappa)$) is expressed as a function of the accumulated plastic strain κ assuming a power law:

$$R(\kappa) = K(e_0 + \kappa)^n \tag{A.2}$$

where e_0, K and n are parameters to be identified.

The yield surface is then expressed following [51] as:

$$\Phi = \sigma_\star - R(\kappa)$$

where $\sigma_\star$ is an effective stress measure depending on both the stress tensor and the void volume fraction, which is the only damage varible. In the case of the GTN

model, the effective scalar stress is implicitly defined as:

$$G(\boldsymbol{\sigma}, f, \sigma_\star) = \frac{\sigma_{\text{eq}}^2}{\sigma_\star^2} + 2q_1 f_\star \cosh\left(\frac{q_2}{2}\frac{\sigma_{kk}}{\sigma_\star}\right) - 1 - q_1^2 f_\star^2 \overset{\text{def}}{=} 0 \tag{A.3}$$

where σ_{eq} is the von Mises stress of the Cauchy stress; σ_{kk} designates its trace; q_1 and q_2 are two parameters and $f_\star$ is a function of porosity. In the present case, $f_\star$ is simply taken equal to the porosity: $f_\star = f_t$. The damage variable f_t can be itself decomposed into two parts which reflect the fact that damage is caused by void nucleation (f_n) and void growth (f_g), so that the void volume fraction is equal to $f_t = f_g + f_n$. The following set of equations gives the evolution of these damage variables:

$$\dot{f}_g = (1 - f_g)\dot{\overline{\omega}} \tag{A.4}$$

$$\dot{f}_n = A_n(\overline{\kappa})\dot{\overline{\kappa}} \tag{A.5}$$

where A_n is a function chosen to be constant (A_n) when the nonlocal cumulated plastic strain reaches a threshold $\overline{\kappa}_c$:

$$A_n(\overline{\kappa}) = \begin{cases} A_n & \text{if} \quad \overline{\kappa} > \overline{\kappa}_c \\ 0 & \text{otherwise} \end{cases} \tag{A.6}$$

Notations $\dot{\overline{\omega}}$ and $\dot{\overline{\kappa}}$ designate the two nonlocal variables that are respectively the regularized forms of the volume variation $\omega = \text{trace}(\boldsymbol{\varepsilon}_p)$ and the effective accumulated plastic strain κ according to the implicit gradient methodology proposed in [7, 59, 60]. Their evolution within the considered material body Ω is governed by the following Helmholtz-type equations involving two characteristic lengths l_ω and l_κ:

$$\overline{\omega} - l_\omega^2 \Delta\overline{\omega} = \omega \quad \text{in} \quad \Omega \tag{A.7}$$

$$\overline{\kappa} - l_\kappa^2 \Delta\overline{\kappa} = \kappa \quad \text{in} \quad \Omega \tag{A.8}$$

with the following natural boundary conditions:

$$\vec{\nabla}\overline{\omega}.\vec{n} = 0 \quad \text{on} \quad \partial\Omega \tag{A.9}$$

$$\vec{\nabla}\overline{\kappa}.\vec{n} = 0 \quad \text{on} \quad \partial\Omega \tag{A.10}$$

where $\partial\Omega$ and $\vec{n}$ respectively designate the boundary of the body Ω and its outer normal vector.

The plastic strain rate tensor $\dot{\boldsymbol{\varepsilon}}_p$ is obtained using the normality rule:

$$\dot{\boldsymbol{\varepsilon}}_p = (1 - f_t)\dot{\kappa}\frac{\partial\Phi}{\partial\boldsymbol{\sigma}} = (1 - f_t)\dot{\kappa}\frac{\partial\sigma_\star}{\partial\boldsymbol{\sigma}} = (1 - f_t)\dot{\kappa}\boldsymbol{n} \tag{A.11}$$

where $\boldsymbol{n}$ designates the normal to the yield surface. Using this expression, the following equivalence between the macroscopic (left hand-side) and the microscopic (right hand-side) plastic dissipations is obtained as:

$$\dot{\boldsymbol{\varepsilon}}_p : \boldsymbol{\sigma} = (1 - f_t)\dot{\kappa}\sigma_\star \tag{A.12}$$

as $\sigma_\star$ is an homogeneous function of order 1 of $\boldsymbol{\sigma}$.

It is assumed that the considered material can exhibit a slight strain rate dependence, so that $\dot{\kappa}$ is expressed as:

$$\dot{\kappa} = \mathcal{F}(\phi) = \dot{p}_0 \left\langle \frac{\sigma_\star - R}{\sigma_0} \right\rangle^{n_v} \tag{A.13}$$

where $\langle . \rangle$ is the positive part function and n_v, $\dot{p}_0$ and σ_0 are material parameters.

Appendix A.2. Finite strain framework

To use this model within a finite strain framework, a corotational formulation [61] is used. The corotational frame is defined using the rotation tensor $\boldsymbol{Q}$ such that:

$$\dot{\boldsymbol{Q}} = \boldsymbol{W}.\boldsymbol{Q} \quad \text{with} \quad \boldsymbol{Q}(t = 0) = \mathbf{1} \tag{A.14}$$

where the $\boldsymbol{W}$ tensor designates the skew-symmetric part of the velocity gradient tensor $\boldsymbol{L}$. The symmetric part of the velocity gradient tensor is denoted $\boldsymbol{D}$ so that: $\boldsymbol{L} = \boldsymbol{D} + \boldsymbol{W}$. From the rate of deformation $\boldsymbol{D}$, one gets the material deformation rate through the following expression:

$$\dot{\boldsymbol{\varepsilon}} = \boldsymbol{Q}^T.\boldsymbol{D}.\boldsymbol{Q} \tag{A.15}$$

Knowing the corotational Cauchy stress (*i.e.*, the Cauchy stress expressed in the coordinate system that rotates with the material), the Cauchy stress in the unrotated frame is given by:

$$\boldsymbol{\Sigma} = \boldsymbol{Q}.\boldsymbol{\sigma}.\boldsymbol{Q}^T \tag{A.16}$$

Appendix A.3. Material parameters

The material parameters used in this paper are identical to the ones identified in [10] for a X70 HSLA (high strength low alloyed) ferritic-pearlitic steel used in modern pipelines, based on results from [50, 51, 57]. They are summarized in the table A.2.

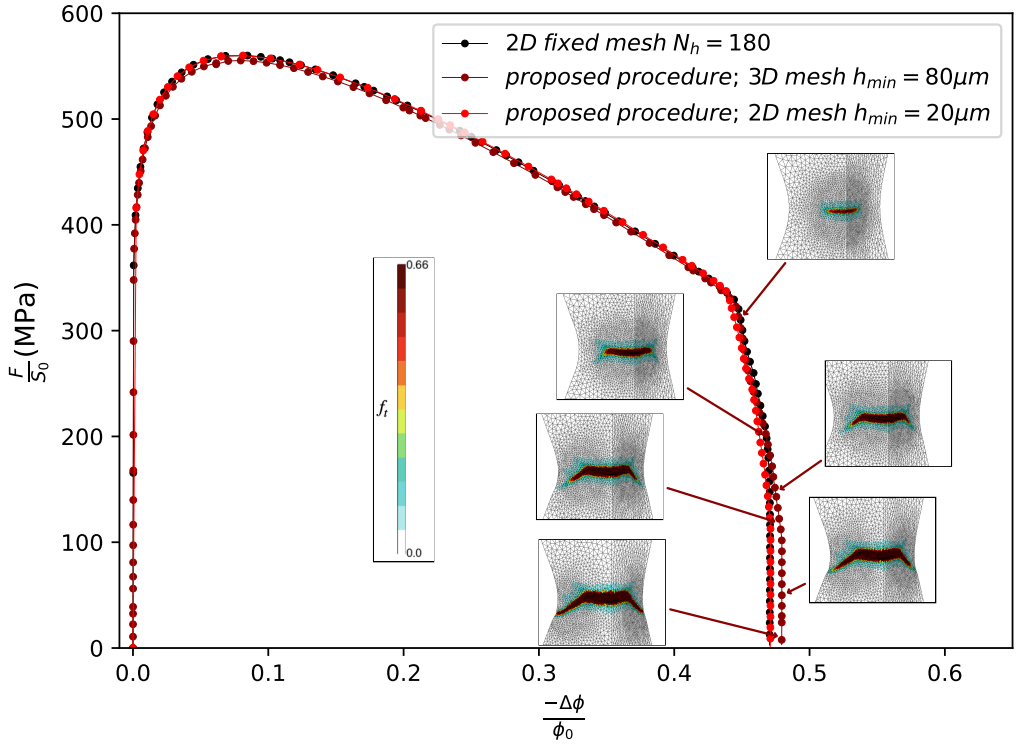

Figure 15: Evolution of the engineering stress as a function of diameter reduction $-\Delta\phi/\phi_0$ for the simulation of a bar with a round cross-section with the proposed approach in 3D (in red), the proposed approach with 2D axisymmetric elements and a smaller minimum element size (in green) and a fixed mesh with 2D axisymmetric elements (in black). All global responses are similar, which tends to indicate the validity of the used 3D mesh. Contours of the total porosity are displayed at different times for the 3D simulation to illustrate the cup–cone crack propagation.

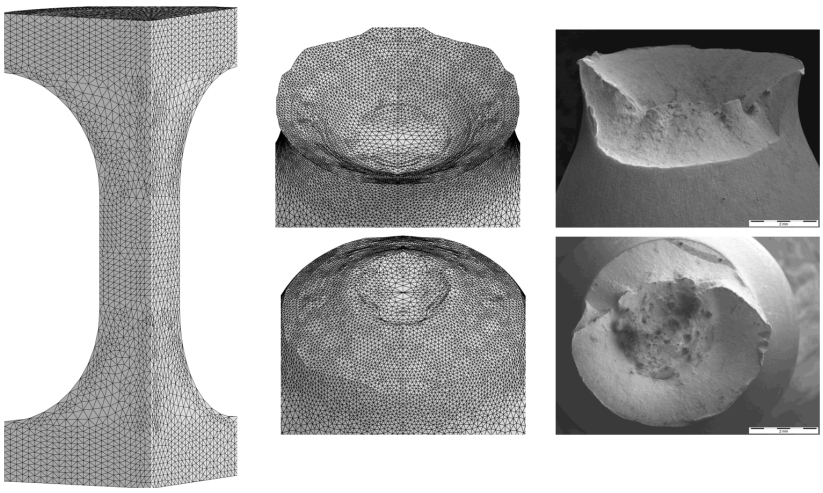

Figure 16: a: Initial mesh of quarter of the specimen for the 3D simulation. b: Fracture surfaces obtained from the 3D simulation. The predicted cup–cone crack surfaces are smooth, well defined and qualitatively in agreement with what can be expected from the experimental results obtained by Besson et al. [57].

Table A.2: Nonlocal GTN material parameters

Young's modulus	E	210GPa
Poisson's ratio	ν	0.3
Isotropic hardening (power law)		
	K	795. MPa.$s^{1/n}$
	e_0	0.002
	n	0.13
Gurson criterion		
	q_1	1.5
	q_2	1.
initial porosity	f_0	$1.5\,10^{-4}$
Strain controlled nucleation		
	A_n	0.4
	$\overline{\kappa}_c$	1.2
Viscous parameters		
	$\dot{p}_0$	$1s^{-1}$
	K	55 MPa
	n_v	5
Non local characteristic lengths		
	l_κ	20 μm
	l_ω	100 μm

References

[1] J. Mediavilla, R.H.J. Peerlings, and M.G.D. Geers. An integrated continuous-discontinuous approach towards damage engineering in sheet metal forming processes. *Eng. Fract. Mech.*, 73(7):895–916, 2006.

[2] Y. Chen, E. Lorentz, A. Dahl, and J. Besson. Simulation of ductile tearing during a full size test using a non local Gurson–Tvergaard–Needleman (GTN) model. *Eng. Fract. Mech.*, 216:108226, 2022.

[3] Z.P. Bazant and G. Pijaudier-Cabot. Non local continuum damage. localization, instability and convergence. *J. Applied Mech.*, 55:287–294, 1988.

[4] S. Forest. Micromorphic approach for gradient elasticity, viscoplasticity, and damage. *J. Eng. Mech.*, 135:117–131, 2009.

[5] E. Lorentz. Ill-posed boundary conditions encountered in 3d and plate finite element simulations. *Finite Elem. Anal. Des.*, 41(11-12):1105–1117, 2005.

[6] G.A. Francfort and J.-J. Marigo. Revisiting brittle fracture as an energy minimization problem. *J. Mech. Phys. Solids*, 46(8):1319–1342, 1998.

[7] R.H.J. Peerlings, R. De Borst, W.A.M. Brekelmans, J.H.P. De Vree, and I. Spee. Some observations on localisation in non–local and gradient damage models. *Eur. J. Mech./A*, 15A(6), 1996.

[8] G. Pijaudier-Cabot and Z. P. Bazant. Nonlocal damage theory. *J. Engrg. Mech.*, 113:1512–1533, 1987.

[9] R. De Borst, L.J. Sluys, H.-B. Muhlhaus, and J. Pamin. Fundamental issues in finite element analyses of localization of deformation. *Engineering Computations*, 10(2):99–121, Jan 1993.

[10] A. El Ouazani Tuhami, S. Feld-Payet, S.a nd Quilici, N. Osipov, and J. Besson. A two characteristic length nonlocal gtn model: Application to cup-cone and slant fracture. *Mech. Mater.*, 171:104350, 2022.

[11] R. El Khaoulani and P.O. Bouchard. An anisotropic mesh adaptation strategy for damage and failure in ductile materials. *Finite Elem. Anal. Des.*, 59:1–10, 2012.

[12] F.T. Yang, A. Rassineux, C. Labergère, and K. Saanouni. A 3d h-adaptive local remeshing technique for simulating the initiation and propagation of cracks in ductile materials. *Comp. Meth. Appl. Mech. Engng*, 330:102–122, 2018.

[13] H.R. Javani, R.H.J. Peerlings, and M.G.D. Geers. Three-dimensional finite element modeling of ductile crack initiation and propagation. *Adv. Model. and Simul. in Eng. Sci.*, pages 3–19, 2016.

[14] J. Mediavilla, R.H.J. Peerlings, and M.G.D. Geers. A robust and consistent remeshing-transfer operator for ductile fracture simulations. *Computers & Structures*, 84(8-9):604–623, 2006.

[15] J. Leclerc, V.D. Nguyen, T. Pardoen, and L. Noels. A micromechanics-based non-local damage to crack transition framework for porous elastoplastic solids. *Int. J. Plasticity*, 127, 2020.

[16] Konstantinos Nikolakopoulos, Jean-Philippe Crété, and Patrice Longère. Progressive failure of ductile metals: Description via a three-dimensional coupled czm–xfem based approach. *Eng. Fract. Mech.*, 243:107498, 2021.

[17] Nicolas Moës, John Dolbow, and Ted Belytschko. A finite element method for crack growth without remeshing. *International Journal for Numerical Methods in Engineering*, 46(1):131–150, 1999.

[18] H. Eldahshan, J. Alves, P.-O. Bouchard, E. Perchat, and E. Pino Munoz. CIPFAR: A 3D unified numerical framework for the modeling of ductile fracture based on the phase field model and adaptive remeshing. *Comp. Meth. Appl. Mech. Engng*, 387:114171, 2021.

[19] H. Eldahshan, P.-O. Bouchard, J. Alves, E. Perchat, and D. Pino Munoz. Phase field modeling of ductile fracture at large plastic strains using adaptive isotropic remeshing. *Computational Mechanics*, 67(3):763–783, 2021.

[20] R. Foerch, J. Besson, G. Cailletaud, and P. Pilvin. Polymorphic constitutive equations in finite element codes. *Comp. Meth. Appl. Mech. Engng*, 141:355–372, 1997.

[21] J. Besson and R. Foerch. Large scale object–oriented finite element code design. *Comp. Meth. Appl. Mech. Engng*, 142:165–187, 1997.

[22] S. Feld-Payet. *Modélisation numérique en mécanique fortement non-linéaire: contact et rupture*, chapter Transition endommagement-fissure. ISTE, 2023.

[23] S. Feld-Payet. *Amorçage et propagation de fissures dans les milieux ductiles non locaux*. PhD thesis, Mines ParisTech, 2010.

[24] S. Feld-Payet, V. Chiaruttini, J. Besson, and F. Feyel. A new marching ridges algorithm for crack path tracking in regularized media. *Int. J. Solids Structures*, 71:57–69, 2015.

[25] V. Chiaruttini, V. Riolo, and F. Feyel. Advanced remeshing techniques for complex 3d crack propagation. In *13th International Conference on Fracture 2013, ICF 2013*, volume 1, 06 2013.

[26] M. Stolarska, D.L. Chopp, N. Moës, and T. Belytschko. Modelling crack growth by level sets in the extended finite element method. *Int. J. Numer. Meth. Engng*, 51:943–960, 2001.

[27] M. Duflot. A study of the representation of cracks with level sets. *Int. J. Numer. Meth. Engng*, 70(11):1261–1302, 2007.

[28] T. Belytschko, H. Chen, J. Xu, and G. Zi. Dynamic crack propagation based on loss of hyperbolicity and a new discontinuous enrichment. *Int. J. Numer. Meth. Engng*, 58(12):1873–1905, 2003.

[29] P. Areias and T. Belytschko. Analysis of three-dimensional crack initiation and propagation using the extended finite element method. *Int. J. Numer. Meth. Engng*, 63:760–788, 2005.

[30] J. Oliver, I.F. Dias, and A.E. Huespe. Crack-path field and strain-injection techniques in computational modeling of propagating material failure. *Comp. Meth. Appl. Mech. Engng*, 274:289–348, 2014.

[31] O. Lloberas-Valls, A.E. Huespe, J. Oliver, and I.F. Dias. Strain injection techniques in dynamic fracture modeling. *Comp. Meth. Appl. Mech. Engng*, 308:499–534, 2016.

[32] E. Tamayo-Mas and A. Rodríguez-Ferran. A medial-axis-based model for propagating cracks in a regularised bulk. *Int. J. Numer. Meth. Engng*, 101(7):489–520, 2015.

[33] E. Tamayo-Mas, J. Feliu-Fabà, M. Casado-Antolin, and A. Rodríguez-Ferran. A continuous-discontinuous model for crack branching. *Int. J. Numer. Meth. Engng*, 120(1):86–104, 2019.

[34] V. Tvergaard and A. Needleman. Analysis of the cup–cone fracture in a round tensile bar. *Acta Metall.*, 32:157–169, 1984.

[35] Umberto De Maio, David Cendón, Fabrizio Greco, Lorenzo Leonetti, Paolo Nevone Blasi, and Jaime Planas. Investigation of concrete cracking phenomena by using cohesive fracture-based techniques: A comparison between an embedded crack model and a refined diffuse interface model. *Theoretical and Applied Fracture Mechanics*, 115:103062, 2021.

[36] Umberto De Maio, Fabrizio Greco, Lorenzo Leonetti, Paolo Nevone Blasi, and Andrea Pranno. A cohesive fracture model for predicting crack spacing and crack width in reinforced concrete structures. *Engineering Failure Analysis*, 139:106452, 2022.

[37] Sam Cuvilliez, Frédéric Feyel, Eric Lorentz, and Sylvie Michel-Ponnelle. A finite element approach coupling a continuous gradient damage model and a cohesive zone model within the framework of quasi-brittle failure. *Computer Methods in Applied Mechanics and Engineering*, 237-240:244–259, 2012.

[38] B. Boroomand and O.C. Zienkiewicz. Recovery procedures in error

estimation and adaptivity. part ii: Adaptivity in nonlinear problems of elasto-plasticity behaviour. *Comp. Meth. Appl. Mech. Engng*, 176:127–146, 1999.

[39] G.T. Camacho and M. Ortiz. Adaptive lagrangian modelling of ballistic penetration of metallic targets. *Comp. Meth. Appl. Mech. Engng*, 142:269–301, 1997.

[40] J. Mediavilla. *Continuous and discontinuous modelling of ductile fracture*. PhD thesis, Technische Universiteit Eindhoven, 2005.

[41] P. Broumand and A.R. Khoei. The extended finite element method for large deformation ductile fracture problems with a non-local damage-plasticity model. *Eng. Fract. Mech.*, 112-113:97 – 125, 2013.

[42] M.R. Javanmardi and M.R. Maheri. Extended finite element method and anisotropic damage plasticity for modelling crack propagation in concrete. *Finite Elem. Anal. Des.*, 165:1–20, 2019.

[43] M.R.R. Seabra, P. Šuštarič, J.M.A. Cesar de Sa, and T. Rodič. Damage driven crack initiation and propagation in ductile metals using xfem. *Computational Mechanics*, 52(1):161–179, 2013.

[44] O. C. Zienkiewicz and J. Z. Zhu. The superconvergent patch recovery and a posteriori error estimates. part 2: Error estimates and adaptivity. *Int. J. Numer. Meth. Engng*, 33(7):1365–1382, 1992.

[45] P. Frey and P. George. *Mesh Generation: Application to Finite Elements: Second Edition*. Wiley, 2008.

[46] A. Simone, G.N. Wells, and L.J. Sluys. From continuous to discontinuous failure in a gradient-enhanced continuum damage model. *Comp. Meth. Appl. Mech. Engng*, 192(41):4581–4607, 2003.

[47] G.W. Stewart. On the early history of the singular value decomposition. *SIAM Review*, 35(4):551–566, 1993.

[48] H. Proudhon, J. Li, F. Wang, A. Roos, V. Chiaruttini, and S. Forest. 3d simulation of short fatigue crack propagation by finite element crystal plasticity and remeshing. *Int. J. of Fat.*, 82:238–246, 2016.

[49] E. Fessler, E. Andrieu, V. Bonnand, V. Chiaruttini, and S. Pierret. Relation between crack growth behaviour and crack front morphology under hold-time conditions in da inconel 718. *Int. J. Fat.*, 96:17–27, 2017.

[50] F. Rivalin. *Développement d'aciers pour gazoducs à haute limite d'élasticité et ténacité élevée : Mécanique et mécanismes de la rupture ductile à grande vitesse.* PhD thesis, École des Mines de Paris, 1998.

[51] J. Besson, D. Steglich, and W. Brocks. Modeling of crack growth in round bars and plane strain specimens. *Int. J. Solids Structures*, 38(46–47):8259–8284, 2001.

[52] A. E. Huespe, A. Needleman, J. Oliver, and P. J. Sanchez. A finite strain, finite band method for modeling ductile fracture. *Int. J. Plasticity*, 28(1):53–69, 2012.

[53] Patrick R Amestoy, Iain S Duff, Jean-Yves L'Excellent, and Jacko Koster. A fully asynchronous multifrontal solver using distributed dynamic

scheduling. *SIAM Journal on Matrix Analysis and Applications*, 23(1):15–41, 2001.

[54] Patrick R Amestoy, Abdou Guermouche, Jean-Yves L'Excellent, and Stéphane Pralet. Hybrid scheduling for the parallel solution of linear systems. *Parallel computing*, 32(2):136–156, 2006.

[55] J.W. Hancock and A.C. Mackenzie. Mechanisms of ductile failure in high-strength steels subjected to multi- axial stress states. *J. Mech. Phys. Solids*, 24:147–160, 1976.

[56] Y. Bao and T. Wierzbicki. On fracture locus in the equivalent strain and stress triaxiality space. *Int. J. Mech. Sci.*, 46(1):81–98, 2004.

[57] J. Besson, D. Steglich, and W. Brocks. Modeling of plane strain ductile rupture. *Int. J. Plasticity*, 19(10):1517–1541, 2003.

[58] Jacques Besson, CN McCowan, and ES Drexler. Modeling flat to slant fracture transition using the computational cell methodology. *Engineering Fracture Mechanics*, 104:80–95, 2013.

[59] M.G.D. Geers, R. de Borst, W.A.M. Brekelmans, and R.H.J. Peerlings. Strain-based transient-gradient damage model for failure analyses. *Comp. Meth. Appl. Mech. Engng*, 160:133–153, 1998.

[60] R.A.B. Engelen, M.G.D. Geers, and F.P.T. Baaijens. Nonlocal implicit gradient-enhanced elasto-plasticity for the modelling of softening behaviour. *Int. J. Plasticity*, pages 403–433, 2003.

[61] F. Sidoroff and A. Dogui. Some issues about anisotropic elastic-plastic models at finite strain. *Int. J. Solids Structures*, 38:9569–9578, 2001.